

RESEARCH ARTICLE

10.1002/2014JC010388

Key Point:

- The carbon budget in seasonal ice is mostly driven by physical processes

Correspondence to:

S. Moreau,
s.moreau@uclouvain.be

Citation:

Moreau, S., M. Vancoppenolle, B. Delille, J.-L. Tison, J. Zhou, M. Kotovitch, D. N. Thomas, N.-X. Geilfus, and H. Goosse (2015), Drivers of inorganic carbon dynamics in first-year sea ice: A model study, *J. Geophys. Res. Oceans*, 120, 471–495, doi:10.1002/2014JC010388.

Received 15 AUG 2014

Accepted 19 DEC 2014

Accepted article online 30 DEC 2014

Published online 29 JAN 2015

Drivers of inorganic carbon dynamics in first-year sea ice: A model study

Sébastien Moreau¹, Martin Vancoppenolle^{1,2}, Bruno Delille³, Jean-Louis Tison⁴, Jiayun Zhou^{3,4}, Marie Kotovitch^{3,4}, David N. Thomas^{5,6}, Nicolas-Xavier Geilfus⁷, and Hugues Goosse¹
¹Georges Lemaître Centre for Earth and Climate Research, Earth and Life Institute, Université catholique de Louvain, Louvain-La-Neuve, Belgium, ²Sorbonne Universités, UPMC, Paris 6, CNRS/IRD/MNHN, Laboratoire d'Océanographie et du Climat, Institut Pierre-Simon Laplace, Paris, France, ³Unité d'Océanographie Chimique, MARE, Université de Liège, Liège, Belgium, ⁴Laboratoire de Glaciologie, Faculté des Sciences, Université Libre de Bruxelles, Bruxelles, Belgium, ⁵Ocean Sciences, College of Natural Sciences, Bangor University, Anglesey, UK, ⁶Marine Research Centre, Finnish Environment Institute, Helsinki, Finland, ⁷Arctic Research Center, Aarhus University, Aarhus, Denmark

Abstract Sea ice is an active source or a sink for carbon dioxide (CO₂), although to what extent is not clear. Here, we analyze CO₂ dynamics within sea ice using a one-dimensional halothermodynamic sea ice model including gas physics and carbon biogeochemistry. The ice-ocean fluxes, and vertical transport, of total dissolved inorganic carbon (DIC) and total alkalinity (TA) are represented using fluid transport equations. Carbonate chemistry, the consumption, and release of CO₂ by primary production and respiration, the precipitation and dissolution of ikaite (CaCO₃·6H₂O) and ice-air CO₂ fluxes, are also included. The model is evaluated using observations from a 6 month field study at Point Barrow, Alaska, and an ice-tank experiment. At Barrow, results show that the DIC budget is mainly driven by physical processes, whereas brine-air CO₂ fluxes, ikaite formation, and net primary production, are secondary factors. In terms of ice-atmosphere CO₂ exchanges, sea ice is a net CO₂ source and sink in winter and summer, respectively. The formulation of the ice-atmosphere CO₂ flux impacts the simulated near-surface CO₂ partial pressure (*p*CO₂), but not the DIC budget. Because the simulated ice-atmosphere CO₂ fluxes are limited by DIC stocks, and therefore <2 mmol m⁻² d⁻¹, we argue that the observed much larger CO₂ fluxes from eddy covariance retrievals cannot be explained by a sea ice direct source and must involve other processes or other sources of CO₂. Finally, the simulations suggest that near-surface TA/DIC ratios of ~2, sometimes used as an indicator of calcification, would rather suggest outgassing.

1. Introduction

Recent observations suggest that the role of sea ice in the marine carbon cycle goes beyond the simple barrier effect suggested by *Morales Maqueda and Rahmstorf* [2002]. Indeed, several active biogeochemical processes have been identified within sea ice [for reviews, see *Loose et al.*, 2011; *Vancoppenolle et al.*, 2013], although their large-scale importance remains largely unevaluated. For instance, calculations by *Rysgaard et al.* [2011] suggest that the decoupling effect of ikaite (CaCO₃·6H₂O) formation on TA and DIC in sea ice could enhance the annual uptake of CO₂ in ice-covered oceans by up to roughly 50%. Confidence in such computations could be improved by better quantification of the various processes driving inorganic carbon dynamics in sea ice.

Ice-atmosphere gaseous CO₂ exchange is possible because of the presence of liquid brine and gas inclusions within the ice. All dissolved constituents, including salts and all forms of inorganic carbon, accumulate in those brines as they are excluded from the crystalline lattice during ice formation [*Papadimitriou et al.*, 2003; *Weeks and Ackley*, 1982]. Indeed, recent field studies report significant sea ice-atmosphere CO₂ fluxes during winter [e.g., *Miller et al.*, 2011], spring, and summer [e.g., *Zemmelink et al.*, 2006]. The measured CO₂ fluxes range from -39.3 to 19.6 mmol m⁻² d⁻¹ from eddy covariance measurements [*Semiletov et al.*, 2004], and from -4 to +2 mmol m⁻² d⁻¹ when using chamber measurements [*Delille*, 2006]. Whereas different flux measurement methods do not agree on the actual flux values (chambers versus eddy-correlation fluxes), the seasonal pattern—CO₂ release by sea ice to the atmosphere in the cold season and atmospheric CO₂ uptake by sea ice in the warming season—seems robust [*Delille et al.*, 2014; *Geilfus et al.*, 2013; *Miller*

et al., 2011; Nomura et al., 2010a, 2010b; Papakyriakou and Miller, 2011]. Nomura et al. [2006] argue that the CO₂ flux has its origin in the seasonal cycle of the CO₂ partial pressure (pCO₂) gradient between the atmosphere and the sea ice brine inclusions near the ice surface.

The pCO₂ value in near-surface brine is therefore a key parameter driving ice-atmosphere carbon exchanges. Surface brine pCO₂ is controlled by the complex dynamics of the carbonate system in sea ice brine implying various physical, chemical, and biological processes. During the cold season, the contraction of brine inclusions due to cooling increases the concentration of solutes, including CO₂ and other gases within brine, and also leads to the formation of gas bubbles since the solubility decreases with temperature [Tison et al., 2002]. Low temperatures and high brine salinities further force the carbonate system toward higher CO₂ brine concentrations [Papadimitriou et al., 2003]. Low temperatures and high brine salinities also promote the precipitation of ikaite [Dieckmann et al., 2008, 2010; Rysgaard et al., 2012, 2013] which increases CO₂ brine concentration. In contrast, during the warming season, brine dilution, net carbon uptake by growing ice algae [Arrigo et al., 2010] and the dissolution of ikaite [Rysgaard et al., 2012, 2007] combine to decrease the brine pCO₂ and enhance the uptake of atmospheric CO₂ by sea ice [Geilfus et al., 2013; Nomura et al., 2010a, 2013; Semiletov et al., 2004].

The goal of the present study was to identify the key physical and biogeochemical processes driving CO₂ dynamics within sea ice and the ice-atmosphere CO₂ fluxes, using a one-dimensional halothermodynamic sea ice model. Our analyses are based on a series of model simulations, run for an observational site at Point Barrow (Alaska) for which a field study was performed in 2009, and for an experimental ice-tank study, where sea ice was grown under controlled conditions.

2. The Model

A module describing carbonate system parameters as prognostic variables has been included in a one-dimensional thermodynamic sea ice model. The model includes the most relevant processes, be they physical (ice growth and melt, temperature, and salinity profiles driving brine dynamics and CO₂ fluxes) or biogeochemical (precipitation/dissolution of ikaite and net primary production).

The *physical component* of the model follows the generic framework introduced by Maykut and Untersteiner [1971] in the energy-conserving implementation of Bitz and Lipscomb [1999] and includes brine dynamics based on Vancoppenolle et al. [2010]. Sea ice is represented by multiple layers of thickness h_i/N , where N is the number of layers, and covered by a snow layer of depth h_s . Sea ice is characterized by vertical temperature (T) and bulk salinity (S) profiles. Temperatures are updated by solving the heat diffusion equation. Changes in ice thickness and snow depth are derived from the interfacial heat budgets, computed from oceanic, inner ice, and atmospheric conductive heat fluxes [Vancoppenolle et al., 2007]. Changes in ice salinity are derived from salt advection-diffusion equations simulating natural brine convection and percolation [Vancoppenolle et al., 2010], and affect the sea ice thermal properties [Bitz and Lipscomb, 1999]. Brine inclusions are assumed to be in thermal equilibrium with the pure ice, hence brine salinity σ and volume fraction e can be directly diagnosed from S and T [Vancoppenolle et al., 2010]. The thermodynamic formulation relies on a linear dependence between brine salinity (σ , g kg⁻¹) and temperature [see Bitz and Lipscomb, 1999], which well approximates the energetics of the system [Notz, 2005]. However, the formulation largely overestimates σ at low temperature, which has undesired chemical consequences. Hence, when computing equilibrium carbonate chemistry, we use the following third-order fit [Assur, 1958; Notz, 2005] for brine salinity:

$$\sigma = -21.4 T - 0.886 T^2 - 0.0107 T^3 \quad (1)$$

Radiative transfer describes the exponential attenuation of the solar radiation that penetrates through the ice below the surface [Bitz and Lipscomb, 1999].

Several passive *biogeochemical tracers* are considered in the model (see Figure 1). They include the two master carbonate system variables, dissolved inorganic carbon (DIC) and total alkalinity (TA) as well as ikaite concentration. The tracer concentrations respond to physical and biogeochemical processes, i.e., net primary production and the precipitation and dissolution of ikaite minerals. A series of additional tracers are considered in the primary production module (described in Appendix A, as biological processes are not the primary focus here).

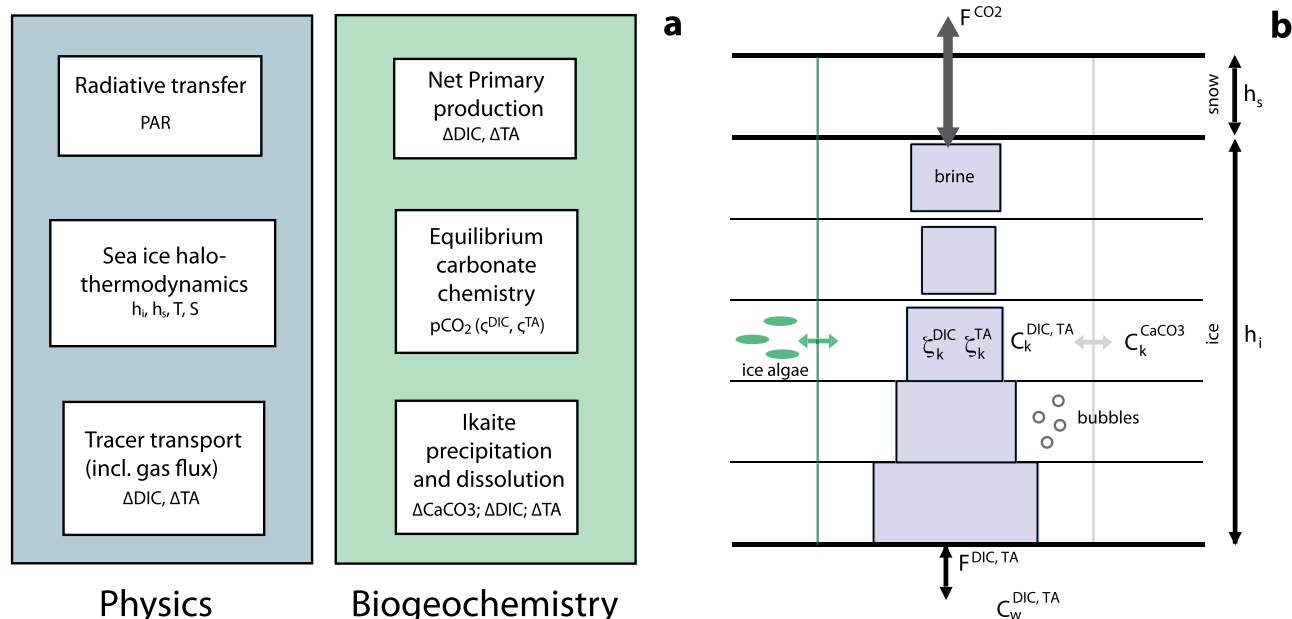
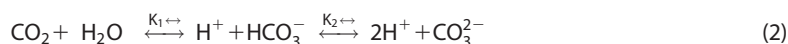


Figure 1. Schematic representation of (a) the processes affecting inorganic carbon dynamics in the model and the related variables (DIC, TA, CaCO_3 , in mmol m^{-3} and pCO_2 , μatm); and of (b) the vertical grid used, where C_k ($k = 1, \dots, N$) refer to bulk (=ice + brine) tracer concentrations and ζ_k to brine concentrations in the k th layer. h_i is the ice thickness, h_s the snow depth, F^{CO_2} the ice-atmosphere CO_2 flux, $F^{\text{DIC,TA}}$ the ice-ocean DIC and TA fluxes, and $C_w^{\text{DIC,TA}}$ the seawater DIC and TA concentrations.

The numerical scheme follows earlier developments [see Moreau *et al.*, 2014; Vancoppenolle *et al.*, 2010]. To make sure TA and DIC are properly conserved, conservation of the total DIC and TA content is checked at the end of each model time step. Ten vertical ice layers discretize the vertical dimension; the time step is 1 h.

2.1. Equilibrium Carbonate Chemistry

The equilibrium chemistry of the carbonate system is central to inorganic carbon dynamics since it links pCO_2 to DIC and TA and hence determines the ice-atmosphere CO_2 exchange. We only summarize the general principles, explaining how they apply to brine in the model and refer the reader to Zeebe and Wolf-Gladrow [2001] for an exhaustive description of the topic. The CO_2 dissolved in brine reacts with water molecules and dissociates into various chemical species:



These chemical reactions are characterized by equilibrium constants (K_1 and K_2) which depend on the brine salinity and temperature. These constants have not yet been measured properly in the range of temperature and salinity found within sea ice brines. Hence, following Delille *et al.* [2007], we evaluate these constants in brine by extrapolating the seawater expressions. K_1 and K_2 are thus computed using the equations of Mehrbach *et al.* [1973] refitted by Dickson and Millero [1987], which perform relatively well in terms of pCO_2 retrievals from TA and DIC in brine [Brown *et al.*, 2014].

To characterize the carbonate system, we use DIC and TA as master variables (as done in Ocean General Circulation Models, see, e.g., Orr *et al.* [2001]), because they are conservative under changes in temperature, salinity, and pressure. DIC and TA are defined as:

$$\text{DIC} = [\text{CO}_{2,\text{aq}}] + [\text{HCO}_3^-] + [\text{CO}_3^{2-}] \quad (3)$$

$$\begin{aligned} \text{TA} &= [\text{HCO}_3^-] + 2*[\text{CO}_3^{2-}] + [\text{OH}^-] - [\text{H}^+] + [\text{B}(\text{OH})_4^-] + \text{minor bases} \\ &= [\text{Na}^+] + [\text{K}^+] + 2[\text{Mg}^{2+}] + 2[\text{Ca}^{2+}] + \\ &\quad \text{minor cations} - [\text{Cl}^-] - 2[\text{SO}_4^{2-}] - [\text{Br}^-] - [\text{NO}_3^-] - \text{minor anions} \end{aligned} \quad (4)$$

DIC is the sum of dissolved inorganic forms of carbon. TA can be viewed as the capacity of the brine to neutralize acids (sum of weak bases), or equivalently as the sum of conservative ions dissolved in solution. The

other carbonate system parameters of interest ($p\text{CO}_2$, CO_2 , HCO_3^- , and CO_3^{2-}) can be derived from TA, DIC, S, and T, assuming chemical equilibrium (a reasonable assumption as the time to reach equilibrium is a few hundreds of seconds, much less than the 1 h model time step). Pressure effects on carbonate chemistry constants are also neglected, assuming that pressure in sea ice does not significantly depart from atmospheric values.

2.2. Tracer Framework

Particulate tracers, such as ikaite do not move with brine motion and remain where they form [as indicated by microscope observations by *Light et al.*, 2003; *Rysgaard et al.*, 2013]. DIC and TA are treated as passive tracers for transport and diffusion. TA is considered as a dissolved tracer, transported in the same way as salt via moving brine. DIC combines dissolved ($\text{CO}_{2,\text{aq}}$, HCO_3^- , and CO_3^{2-}) and gas properties ($\text{CO}_{2,\text{g}}$), thus it is transported in the same way as salt via moving brine but also forms gas bubbles and exchanges at the brine-atmosphere interface [*Moreau et al.*, 2014].

Following the general framework for sea ice tracers introduced in *Vancoppenolle et al.* [2013], the bulk concentrations of nonparticulate tracers (C^{DIC} and C^{TA}) can be broken down into brine and gas bubble contributions:

$$C^n = e \zeta^n + C^{\text{b},n} \quad (5)$$

Here e is brine volume fraction, ζ^n is the concentration in brine of the n th tracer of interest. The bulk concentration of gas in bubbles, $C^{\text{b},n}$, is relevant to gas tracers only (e.g., $\text{CO}_{2,\text{g}}$, hence DIC). Changes in C^{DIC} , C^{TA} , and C^{CaCO_3} are separated into physical (S^{p}) and biogeochemical (S^{b}) contributions:

$$\frac{\partial C}{\partial t} = S^{\text{p}} + S^{\text{b}} \quad (6)$$

which will be discussed below.

In order to assess the impact of physical and biogeochemical processes, the net DIC and TA budgets over the sea ice growth/melt period were computed as the change in DIC and TA stocks ($M^{\text{DIC}} = \int_0^h C^{\text{DIC}}(z) dz$ and $M^{\text{TA}} = \int_0^h C^{\text{TA}}(z) dz$ in mmol m^{-2}) between two instants t_0 and t_1 :

$$[M^{\text{DIC}}]_{t_0}^{t_1} = GM + BD + AB + \beta \quad (7)$$

$$[M^{\text{TA}}]_{t_0}^{t_1} = GM + BD + \beta \quad (8)$$

The terms on the right side refer to the time-integral contributions of growth and melt (GM), brine drainage (BD), air-brine flux (AB), and biogeochemical processes (β).

2.3. Physical Processes

Ice growth and melt, as well as brine and gas dynamics affect model tracers. Following *Vancoppenolle et al.* [2010], the uptake of DIC and TA during basal growth is proportional to seawater concentration (C_w) and the growth rate. Conversely, the release of DIC and TA during melting (surface or basal) is proportional to the local bulk ice DIC and TA concentration and melt rate. DIC and TA are diffused and advected by brine convection and percolation, as formulated by *Vancoppenolle et al.* [2010]. Gas processes—namely gas bubble formation and ice-atmosphere fluxes—were derived from *Moreau et al.* [2014].

The *brine-gas bubbles* CO_2 flux directly affects DIC and is proportional to the saturation of CO_2 within the brine. In addition, the formation of gas bubbles is subject to the condition that the pressure of the four major atmospheric gases (N_2 , O_2 , Ar , and CO_2) in brine exceeds the brine hydrostatic pressure. Gas bubbles do not follow brine dynamics and, instead rise once the brine network is connected.

The *ice-atmosphere* CO_2 flux directly affects DIC, but not TA. Following *Nomura et al.* [2006], we assumed this exchange as (i) proportional to the CO_2 partial pressure ($p\text{CO}_2$) difference between brine and the atmosphere, (ii) proportional to the near-surface brine volume, and (iii) not influenced by snow (we assume gas concentrations in snow in equilibrium with the atmosphere). Based on these assumptions, the ice-atmosphere CO_2 flux reads:

$$F^{\text{CO}_2} = k^{\text{CO}_2} * e * (\zeta^{\text{CO}_2} - K_0 f^{\text{CO}_2}) \quad (9)$$

Here k^{CO_2} (m/s) is the gas exchange velocity, e the near-surface brine volume fraction, ζ^{CO_2} the concentration of CO_2 in brine (mmol/m³), and f^{CO_2} the atmospheric CO_2 fugacity (atm). We consider $f^{\text{CO}_2} = p_{\text{atm}} * 0.00038$, with p_{atm} the atmospheric pressure and 380 ppmV a mixing ratio [see *Sarmiento and Gruber, 2006*; Table 3.1.1, p. 74]. To estimate the CO_2 exchange velocity, we used the stagnant film assumption:

$$k^{\text{CO}_2} = D / z_{\text{BL}} \quad (10)$$

D ($= 0.94 \times 10^{-9} \text{ m}^2 \text{ s}^{-1}$) is the molecular diffusion coefficient of dissolved CO_2 [Broecker and Peng, 1974], in agreement with observations in sea ice [Crabeck et al., 2014] and z_{BL} ($= 0.5 \mu\text{m}$) is the thickness of the diffusive boundary layer. In practise, this surface flux formulation is convenient because, first, it contains the basic physical dependencies and second, the average magnitude of ice-atmosphere CO_2 fluxes can be tuned by varying z_{BL} .

We acknowledge that this parameterization neglects several physical processes (e.g., the role of snow as a CO_2 reservoir, wind pumping). It also ignores complex permeability effects. In section 4.3, the impact of a brine volume fraction threshold eth below which the ice-atmosphere CO_2 flux is imposed to be zero is tested.

2.4. Biogeochemical Source and Sink Processes

The sources and sink terms corresponding to biogeochemical processes for inorganic carbon dynamics are associated with (i) primary production and respiration; and (ii) ikaite precipitation and dissolution.

Net primary production (NPP = photosynthesis—respiration, in carbon units) affects both DIC and TA. First, DIC increases (decreases) due to photosynthesis (respiration), which, assuming a constant 1:1 Redfield ratio, consumes (releases) 1 mole of CO_2 (hence of DIC) for the production of 1 mole of organic carbon, hence:

$$\left. \frac{\partial \text{C}^{\text{DIC}}}{\partial t} \right|_{\text{NPP}} = - \text{NPP} \quad (11)$$

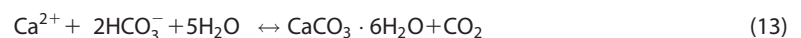
Second, NPP affects TA, through nitrate (NO_3^-) uptake or release. Each mole of organic carbon produced (removed) through photosynthesis (respiration) is assumed to consume 16/106 moles of NO_3^- in the model [Redfield et al., 1963]. Since NO_3^- directly and negatively contributes to TA (equation (4)) [Zeebe and Wolf-Gladrow, 2001], 1 mole of organic carbon produced (removed) increases (reduces) TA by 16/106 moles:

$$\left. \frac{\partial \text{C}^{\text{TA}}}{\partial t} \right|_{\text{NPP}} = 16/106 \text{ NPP} \quad (12)$$

NPP is simulated using a simple N-P (nutrient-phytoplankton) module with light and nutrient limitations, temperature, and brine salinity effects and is coupled to brine dynamics as described in Appendix A.

2.5. Calcium Carbonate Precipitation and Dissolution

Under certain conditions, calcium (Ca^{2+} , one of the major seawater salts) and CO_3^{2-} brine concentrations increase above the saturation threshold of ikaite ($\text{CaCO}_3 \cdot 6\text{H}_2\text{O}$). Consequently, ikaite precipitates within sea ice following:



Precipitation and dissolution of ikaite affects both DIC and TA, as seen from equation (13): the precipitation (dissolution) of 1 mole of ikaite consumes (releases) 2 moles of HCO_3^- and releases (consumes) 1 mole of CO_2 , which (i) decreases (increases) DIC by 1 mole and (ii) decreases (increases) TA by 2 moles, since HCO_3^- contributes by one negative units to TA (equation (4)). In summary, changes in DIC and TA directly depend on the net precipitation/dissolution of ikaite crystals, S^{CaCO_3} :

$$\left. \frac{\partial \text{C}^{\text{DIC}}}{\partial t} \right|_{\text{ika}} = - S^{\text{CaCO}_3} \quad (14)$$

$$\left. \frac{\partial C^{TA}}{\partial t} \right|_{ika} = -2 S^{CaCO_3} \quad (15)$$

The factors driving ikaite precipitation and dissolution in sea ice are not yet fully understood. According to present knowledge, we assume ikaite precipitation (dissolution) if the saturation state of brine $\Omega > 1$ ($\Omega < 1$). The saturation state of brine Ω is the ratio:

$$\Omega = \frac{\zeta^{Ca^{2+}} \times \zeta^{CO_3^{2-}}}{K_{sp}} \quad (16)$$

where the solubility product $K_{sp}(T)$ ($= 10^{-pK_{sp}}$) follows the laboratory measurements of *Papadimitriou et al.* [2013]:

$$pK_{sp} = 15489.09608 - \frac{623443.70216}{T} - 2355.14596 \ln(T) \quad (17)$$

which is valid for brine in thermal equilibrium with the surrounding pure ice at its freezing point (hence the dependence in brine salinity is implicit).

Here, it is assumed that the precipitation/dissolution rates (in $\text{mmol ikaite m}^{-3} \text{ h}^{-1}$) are proportional to the saturation of carbonate: the difference between the carbonate concentration in brine ($\zeta^{CO_3^{2-}}$) and the carbonate saturating concentration in brine ($= K_{sp} / \zeta^{Ca^{2+}}$). In addition, the inverse of a time constant T^{CaCO_3} (100 h) is used to calibrate the intensity of the process (see section 3.3):

$$S^{CaCO_3} = e \left(\zeta^{CO_3^{2-}} - \frac{K_{sp}}{\zeta^{Ca^{2+}}} \right) / T^{CaCO_3} \quad (18)$$

Whereas Ca^{2+} is explicitly simulated, in practice our simulations suggest that it could as well be prescribed since its high concentration in brine (estimated between 15 and 100 mol m^{-3}) is not able to limit ikaite precipitation.

2.6. Diagnosed Variables

In the model, pCO_2 is diagnosed from the dissolved CO_2 concentration (mmol m^{-3}), which is derived from DIC, TA, T, and S, and from the solubility of CO_2 , K_0 ($\text{mmol m}^{-3} \text{ atm}^{-1}$), which is evaluated using the expression of *Weiss* [1974]:

$$pCO_2 = \frac{CO_2}{K_0} \quad (19)$$

The model bulk DIC and TA concentrations correspond to *filtered* DIC and TA concentrations reported in the observational literature. In the laboratory, such values are mostly obtained by filtration of the samples before measurement, which excludes ikaite crystals. In the model, as bulk DIC and TA concentrations do not include the contribution of ikaite, they are considered to best match *filtered* observational values. *Nonfiltered* DIC and TA (DIC_{nf} and TA_{nf} , including ikaite crystals) are sometimes reported in the observational literature. Corresponding *nonfiltered* model values (DIC_{nf} and TA_{nf}) can be diagnosed by adding $1 \times$ and $2 \times$ the ikaite concentration to, respectively, DIC and TA. Unless explicitly mentioned, the DIC and TA concentrations reported in this manuscript correspond to *filtered* values.

3. Model Setup

3.1. Observations Used for Model Validation

For comparison with the model results, we used two observational data sets: (1) From a field survey on land-fast sea ice at Barrow (Alaska). (2) From an experimental ice-tank study (INTERICE 4) at the Arctic Environmental Test Basin of the Hamburg Ship Model Basin (HSVA-Hamburg, Germany), where sea ice was grown under controlled conditions. The field survey at Barrow was performed from January to June 2009. Ice cores were extracted 1–3 times per month. The physical and biogeochemical properties of the extracted ice cores were measured as in *Geilfus et al.* [2013, 2012] and *Zhou et al.* [2013]. The INTERICE 4 study took place in September–October 2009. A description of the ice growth conditions for INTERICE 4 is given in *Moreau et al.* [2014]. Both experiments used the same measurement protocol.

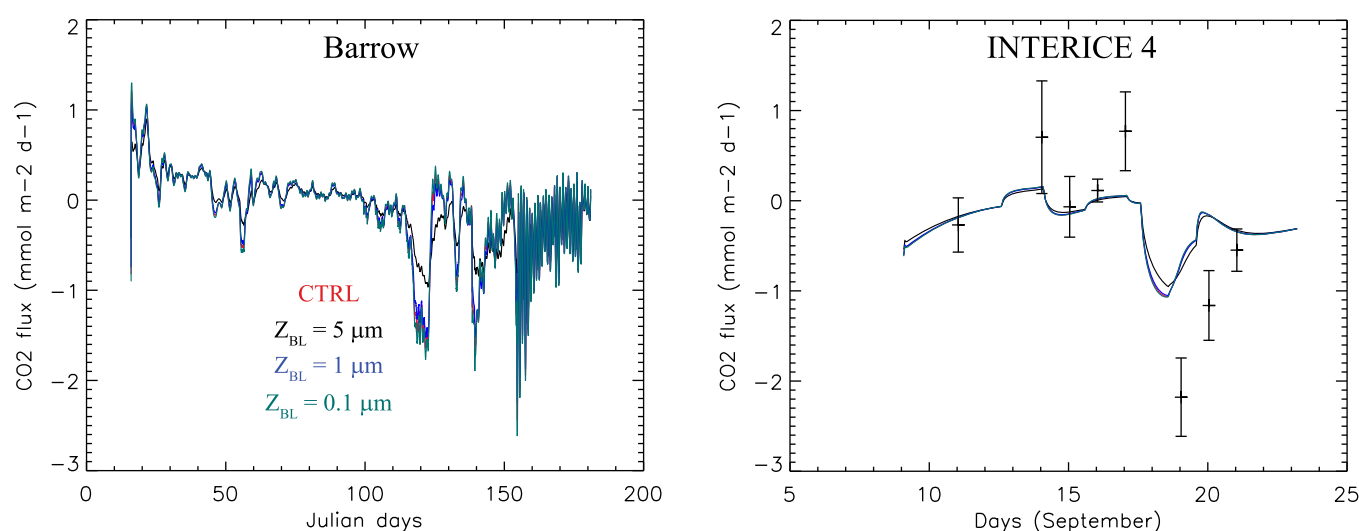


Figure 2. Simulated sea ice-atmosphere CO_2 fluxes ($\text{mmol m}^{-2} \text{d}^{-1}$) for the simulations at (left) Barrow and during (right) INTERICE 4. Simulated CO_2 fluxes are given for the CTRL (red) and runs with boundary layer thickness, z_{BL} , of 5 (black), 1 (blue), and 0.1 (green) μm . Observed CO_2 fluxes \pm standard deviation ($\text{mmol m}^{-2} \text{d}^{-1}$) are plotted for INTERICE 4.

3.2. Forcing and Initialization

At Barrow, the simulation spans 16 January to 30 June 2009 and at INTERICE 4, 9–22 September. The description of the external forcings and of the initial ice conditions for these two simulations is given in Moreau *et al.* [2014], except for the carbonate system. Ideally, observations should be used to specify TA and DIC values in seawater and initial values in sea ice. However, observations were not always available. Hence, we specified TA and DIC value in seawater and initial values in sea ice based on our own in situ observations, the literature and from a model sensitivity analysis to initial conditions discussed in section 4.3. Seawater TA and DIC concentrations were prescribed to 2000 and 2200 mmol m^{-3} at Barrow [source: Bates, 2006; and sensitivity study] and to 2100 and 2400 mmol m^{-3} at INTERICE 4 (source: sensitivity study). Initial sea ice TA and DIC concentrations were set to 300 and 400 mmol m^{-3} at Barrow (source: measurements and sensitivity study) and to 525 and 730 mmol m^{-3} at INTERICE 4 (source: measurements and sensitivity study).

3.3. Model Calibration

The weakly constrained model parameters were adjusted to achieve the best agreement with observations for several model diagnostics. The final parameter values were chosen for our control run (CTRL) for Barrow and INTERICE 4. CO_2 fluxes in the model are calibrated by adjusting z_{BL} , which, in the CTRL is set to 0.5 μm . The goal was to simulate CO_2 fluxes as close as possible to observations during INTERICE 4 and to the literature values for Barrow. At Barrow, the ice-atmosphere CO_2 fluxes simulated in the CTRL range from -2.45 to $1.2 \text{ mmol m}^{-2} \text{d}^{-1}$; at INTERICE 4, they span -1.06 to $0.15 \text{ mmol m}^{-2} \text{d}^{-1}$ (Figure 2). At Barrow, the simulated ice-atmosphere CO_2 flux seasonally evolves over the entire ice season, from outward CO_2 fluxes during ice growth to inward CO_2 fluxes once the surface brine $p\text{CO}_2$ is below the atmospheric 380 μatm value, which occurs once the sea ice surface temperature approaches -8°C . During INTERICE 4, a similar change in CO_2 flux direction is simulated once the temperature increases above -6°C on September 17. This change in the CO_2 flux direction is consistent with measurements. Increasing the boundary layer thickness, z_{BL} , to 1 or 5 μm decreases simulated ice-atmosphere CO_2 fluxes for both experiments (Figure 2). On the contrary, decreasing z_{BL} to 0.1 μm or less does not efficiently increase simulated CO_2 fluxes because of the rapid exhaustion of near-surface DIC by more intense ice-atmosphere fluxes (see section 4.3, for more explanations on the limitation of CO_2 fluxes by DIC stocks).

The CO_2 fluxes simulated at Barrow (-2.45 to $1.2 \text{ mmol m}^{-2} \text{d}^{-1}$) are in the lower range of the chamber observations reported in the literature: -5.4 to $+2 \text{ mmol m}^{-2} \text{d}^{-1}$ [Delille *et al.*, 2007; Geilfus *et al.*, 2013, 2014; Nomura *et al.*, 2010a, 2013, 2010b]. The simulated CO_2 fluxes during INTERICE 4 are also lower than observations. Hence, z_{BL} (0.5 μm) was chosen to maximize CO_2 fluxes.

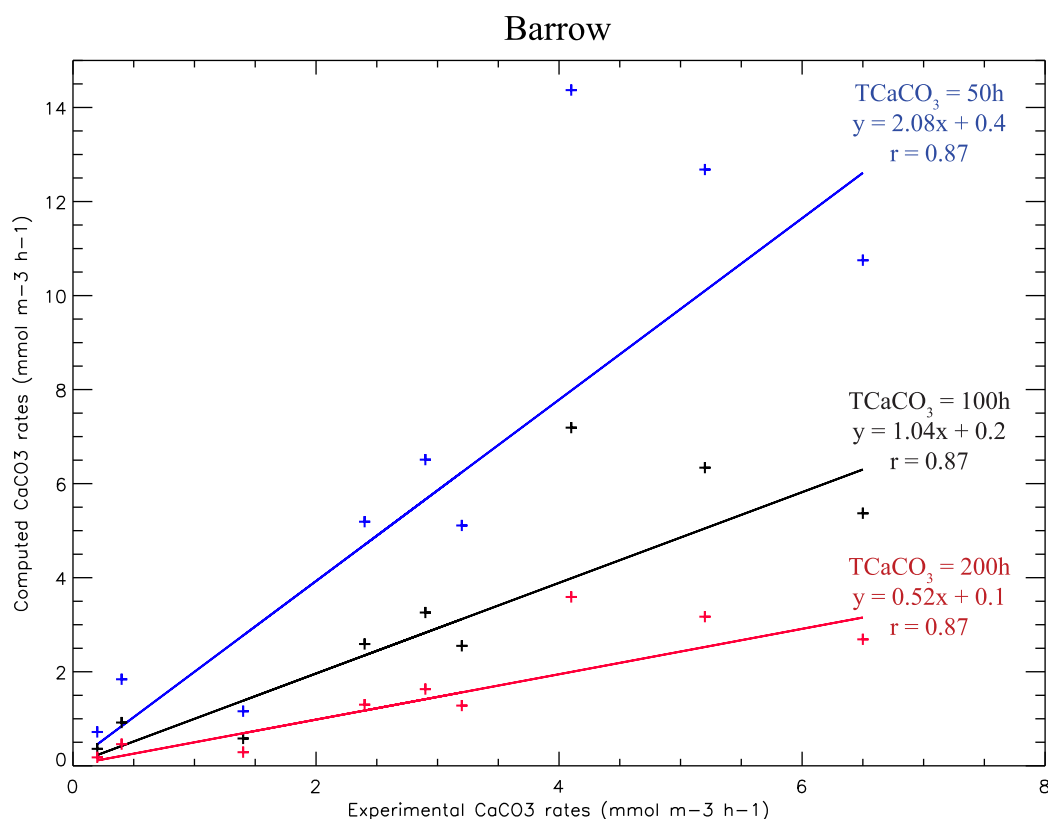


Figure 3. Linear regressions between experimental [Papadimitriou *et al.*, 2014] calcification rates ($\text{mmol m}^{-3} \text{h}^{-1}$), and those computed by the calcification routine, using $T^{\text{CaCO}_3} = 50 \text{ h}$ (blue), $T^{\text{CaCO}_3} = 100 \text{ h}$ (CTRL, black), $T^{\text{CaCO}_3} = 200 \text{ h}$ (red).

The model time scale associated with ikaite precipitation and dissolution (T^{CaCO_3}) was calibrated by comparing simulated rates of ikaite precipitation with the laboratory experiments of Papadimitriou *et al.* [2014]. In these experiments, the ikaite precipitation or dissolution rate was measured on seawater and seawater-derived brine samples, held at subzero temperature for various physical and chemical conditions. These experiments were repeated numerically, by using the same experimental conditions (TA, DIC, CO_3^{2-} , Ca^{2+} , $p\text{CO}_2$, brine temperature, and salinity) as inputs for the calcification subroutine used in our model. The resulting computed values for ikaite precipitation rates were compared with the laboratory observations. There was a significant correlation between the simulated ikaite precipitation rates and the laboratory observations ($r = 0.87$ and $p < 0.01$, Figure 3). The r value was the same when the comparison was repeated for different T^{CaCO_3} because of the linear dependence of ikaite precipitation to T^{CaCO_3} in the model (equation (18)). Thus, the best relationship between the simulated and the experimental ikaite precipitation rates was obtained when the slope of the regression line was as close to 1 as possible, which was obtained with for $T^{\text{CaCO}_3} \sim 100 \text{ h}$. This value was hence retained as a control value. In equation (18), T^{CaCO_3} can be understood as the characteristic time scale of ikaite precipitation and dissolution. This is in the lower range of the time scale for ikaite precipitation to reach equilibrium in sea ice (between 1 and 3 weeks: 216–528 h) calculated by Papadimitriou *et al.* [2014].

Finally, the gross primary production (GPP) integrated over the ice column and over the entire Barrow simulation is 1.3 g C m^{-2} in the CTRL and is in the range of estimations and measurements for sea ice in the Arctic Ocean: Between 0.4 and 15 g C m^{-2} [Deal *et al.*, 2011 and reference therein]. In addition, in the model, Chl-*a* accumulates in the lower part of sea ice as suggested by observations [Arrigo *et al.*, 2010] and as described below.

4. Results

4.1. Sea Ice Mass Balance

At Barrow, the simulated ice grows from January to May. In accordance with observations, ice thickness reaches its maximum—1.29 m—on 27 May (Figure 4). The simulated snow depth initially increases, up to its

Barrow

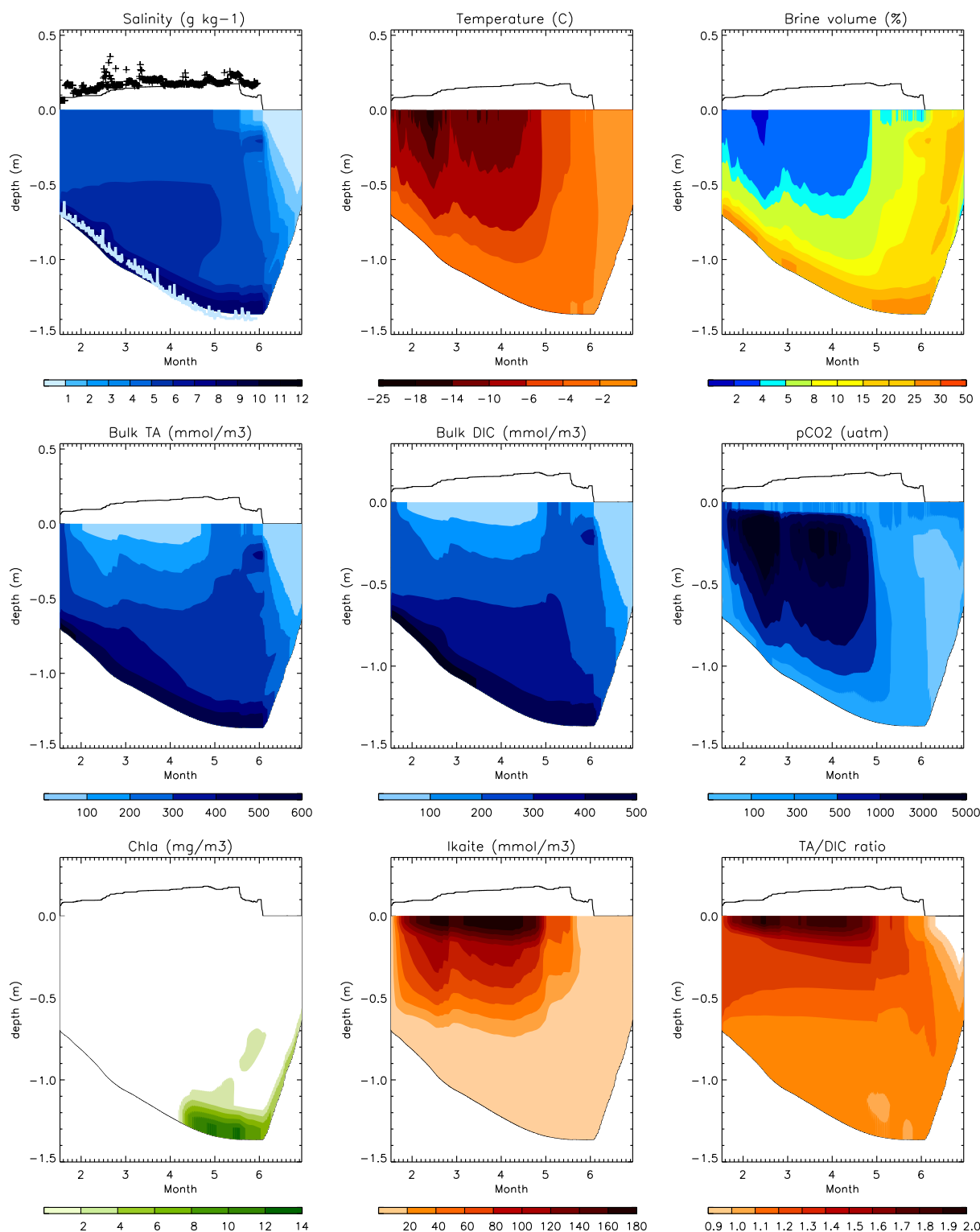


Figure 4. Contoured salinity (g kg^{-1}), temperature ($^{\circ}\text{C}$), brine volume (%), bulk TA (mmol m^{-3}), bulk DIC (mmol m^{-3}), pCO_2 (μatm), bulk Chl- a (mg m^{-3}), bulk ikaite (mmol m^{-3}), and the nonfiltered TA/DIC ratio in the ice domain for the CTRL run at Barrow (Alaska). Horizontal and vertical axes refer to months and depth from the snow ice interface, respectively. Observations of snow depth (black crosses) and ice thickness (light blue dots) are also depicted.

maximum of 0.21 m, which is reached on 25 April. Snow starts melting in mid-May and has fully disappeared by 3 June. The simulated ice salinity, temperature and brine volume profiles compare reasonably well with measurements [see Moreau *et al.*, 2014, Figures 2 and 3]. During ice growth, ice formed at the base by congelation traps salt, which is then released to the ocean through gravity drainage. During surface melting, the meltwater drains the brine network, desalinating the remaining upper ice layers. [Vancoppenolle *et al.*, 2007].

For the INTERICE 4 simulation, sea-ice grows from 9 to 22 September (Figure 5). The maximal ice thickness (0.21 m) is reached on 22 September, as measured. The sea ice is relatively cold until 17 September (i.e., the cold phase, Figure 5), and from then on warms (17–22 September: the warm phase) and becomes permeable to fluid transport [see Moreau *et al.*, 2014, Figure 4, for a presentation of simulated and observed sea ice salinity and temperature profiles]. There was no snow during this experiment.

4.2. The Carbonate System

In this section, we describe the general distribution of bulk ice DIC, TA, $p\text{CO}_2$, Chlorophyll-a (Chl-a), ikaite, and the *nonfiltered* TA/DIC ratio through the sea ice season for the Barrow (Figure 4) and INTERICE 4 (Figure 5) simulations using standard parameters (CTRL, Table 1). At Barrow, bulk DIC and TA follow ice salinity, decreasing from the ice base to the top. Newly formed ice at the base has bulk DIC and TA concentrations closer to seawater values. In the uppermost ice, values are lower due to losses by brine convection and percolation. During ice melt, DIC and TA decrease at all ice depths mostly due to percolation and to a lesser extent due to ikaite dissolution and CO_2 uptake from net primary production. The simulation of bulk sea ice *filtered* and *nonfiltered* TA is reasonable during early spring (8 and 12 May) and summer (5 June, Figure 6), except near the ice surface, where it is underestimated.

In the Barrow simulation, during ice growth, the simulated $p\text{CO}_2$ is high in the upper half of sea ice due to low brine volume and high brine salinity (Figure 4). In the uppermost sea ice layer, $p\text{CO}_2$ stays relatively low during ice growth because of ice-atmosphere CO_2 fluxes (Figure 2). As soon as temperature increases (28 May), the simulated $p\text{CO}_2$ continuously decreases in the ice to the end of the simulation. This decrease in $p\text{CO}_2$ is mostly due to brine dilution and percolation and to a lesser extent due to the onset of the spring ice algae bloom and the dissolution of ikaite crystals. Close to the ice surface, however, the brine $p\text{CO}_2$ is kept at $\sim 375 \mu\text{atm}$ (close to the atmospheric CO_2 partial pressure) due to ice-atmosphere CO_2 fluxes during ice melt. The simulation of $p\text{CO}_2$ in brine compares reasonably well with observations during early spring (8 and 12 May) and summer (5 June, Figure 6) although it is underestimated in the lower half of the ice in summer.

Finally, in the model, a sharp increase in Chl-a occurs in the bottom part of the ice in spring (with a bulk Chl-a concentration $\sim 15 \text{ mg m}^{-3}$ on 8 May). Ikaite precipitates regularly near the surface of the ice during ice growth before it dissolves during ice melt (Figure 4). The precipitation of ikaite stores alkalinity in a latent state and results in a ratio of *nonfiltered* TA/DIC > 1 in the upper half of the ice (Figure 4). The *nonfiltered* TA/DIC ratio increases above > 1.5 near the ice surface since ice-atmosphere CO_2 fluxes additionally reduce the near-surface DIC concentration.

The inorganic carbon dynamics in sea ice at INTERICE 4 are similar to those simulated at Barrow, even though they span a much shorter time period (2 weeks rather than a few months). As in Barrow, the simulated bulk DIC and TA for INTERICE 4 show a similar pattern as salinity (Figure 5), and compare reasonably well with observations during both cold and warm phases (Figure 7), although DIC and TA are slightly underestimated at the base of sea ice during ice growth. The simulated brine $p\text{CO}_2$ is higher than atmospheric values during the cold phase and lower during the warm phase; and compares reasonably well with the observations during both phases (Figure 7) although it is slightly overestimated in the upper part of sea ice during ice growth. This could be due to a too fast increase in the surface ice $p\text{CO}_2$ or underestimated ice-atmosphere CO_2 fluxes between 9 and 14 September.

4.3. Model Sensitivity

The CTRL simulation is characterized by substantial uncertainties, which for some of them may significantly affect the robustness of our results. In order to evaluate the impact of these uncertainties, we analyzed the model sensitivity to initial and boundary conditions, as well as to the strength of several physical and biogeochemical processes, for the Barrow conditions.

INTERICE 4

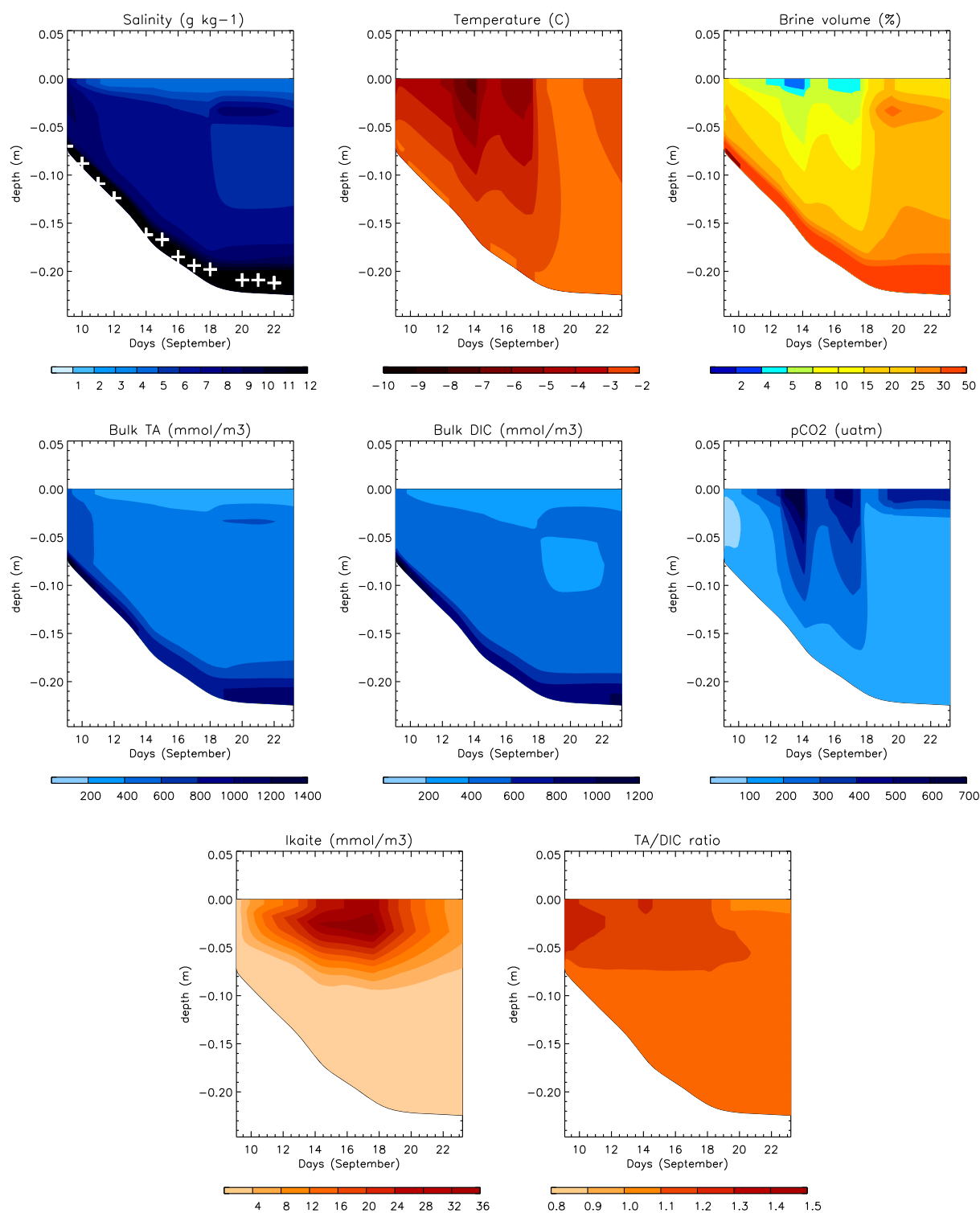


Figure 5. Contoured salinity (g kg^{-1}), temperature ($^{\circ}\text{C}$), brine volume (%), bulk TA (mmol m^{-3}), bulk DIC (mmol m^{-3}), pCO₂ (μatm), bulk ikaite (mmol m^{-3}), and the *nonfiltered* TA/DIC ratio in the ice domain for the CTRL run at INTERICE (an ice tank experiment in Hamburg, Germany). Horizontal and vertical axes refer to days in September and depth from the snow ice interface, respectively. White crosses indicate observed ice thickness.

Table 1. Model Parameters

Variables	Definition	Units	CTRL Value
Z_{BL}	Boundary layer thickness ^a	μm	0.5
eth	Surface brine volume fraction threshold for ice-atmosphere CO_2 flux ^a	%	0
τ_{CaCO_3}	Time constant for CaCO_3 precipitation/dissolution ^b	h	100

^aThis study.

^bThis study in accord with Papadimitriou et al. [2014].

First, the roles of initial and boundary conditions were tested via the analysis of several sensitivity runs (described in Table 2, depicted in Figure 8). The simulated January–February average $p\text{CO}_2$ (arbitrarily chosen to represent the role of initial conditions) is highly sensitive to changes in the initial value of the TA/DIC ratio in sea ice (Figure 8a): A high/low sea ice TA/DIC ratio involves an increase/decrease in brine pH, which significantly decreases/increases the average January–February $p\text{CO}_2$. The equilibrium of the carbonate

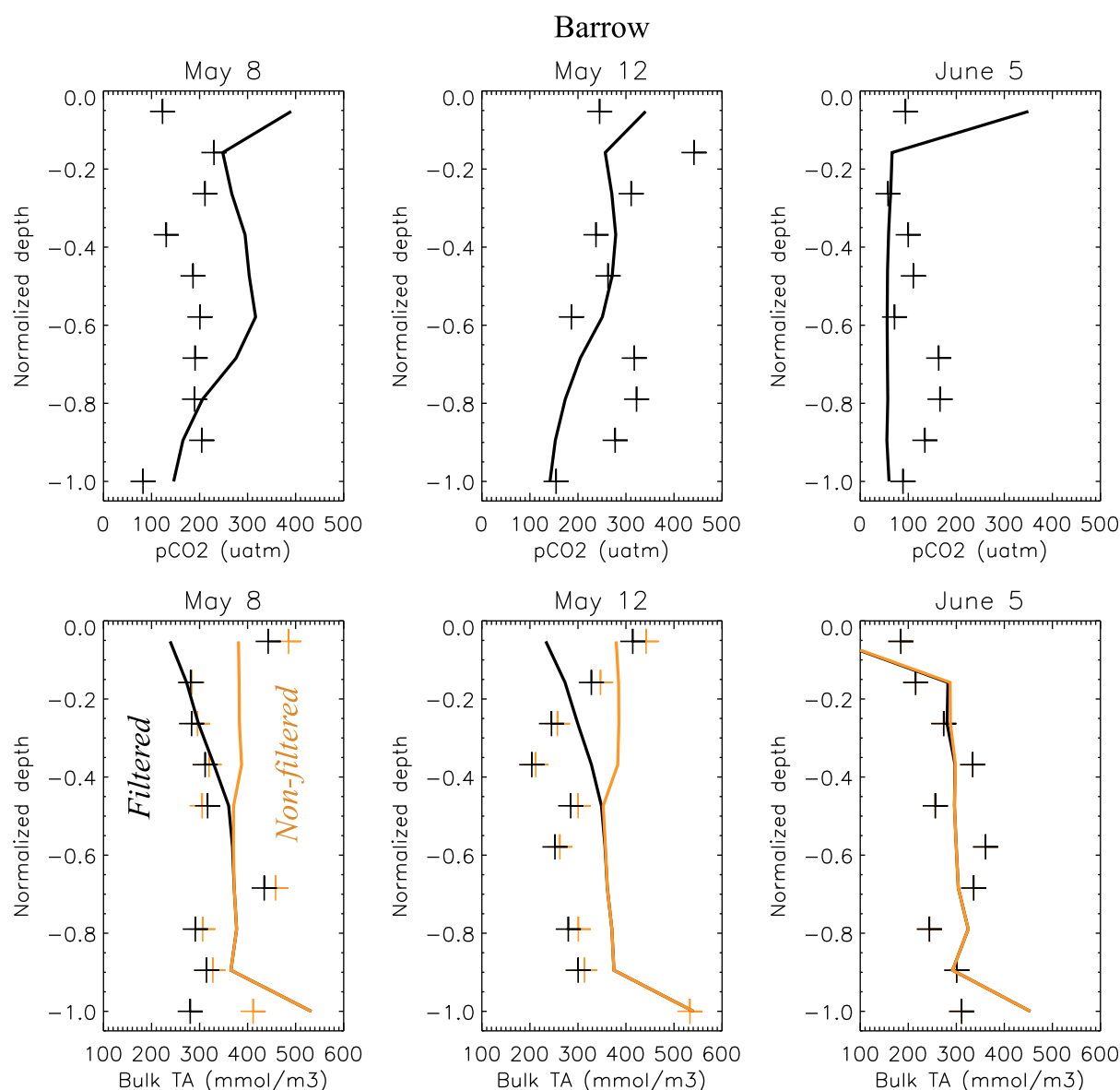


Figure 6. (top) Normalized vertical profiles of $p\text{CO}_2$ (μatm), from the CTRL simulation (lines) and corresponding observations (symbols), for three spring stations at Barrow. (bottom) Same, but for bulk TA concentration (mmol m^{-3}), filtered (black) and nonfiltered (i.e., including CaCO_3 contribution, orange).

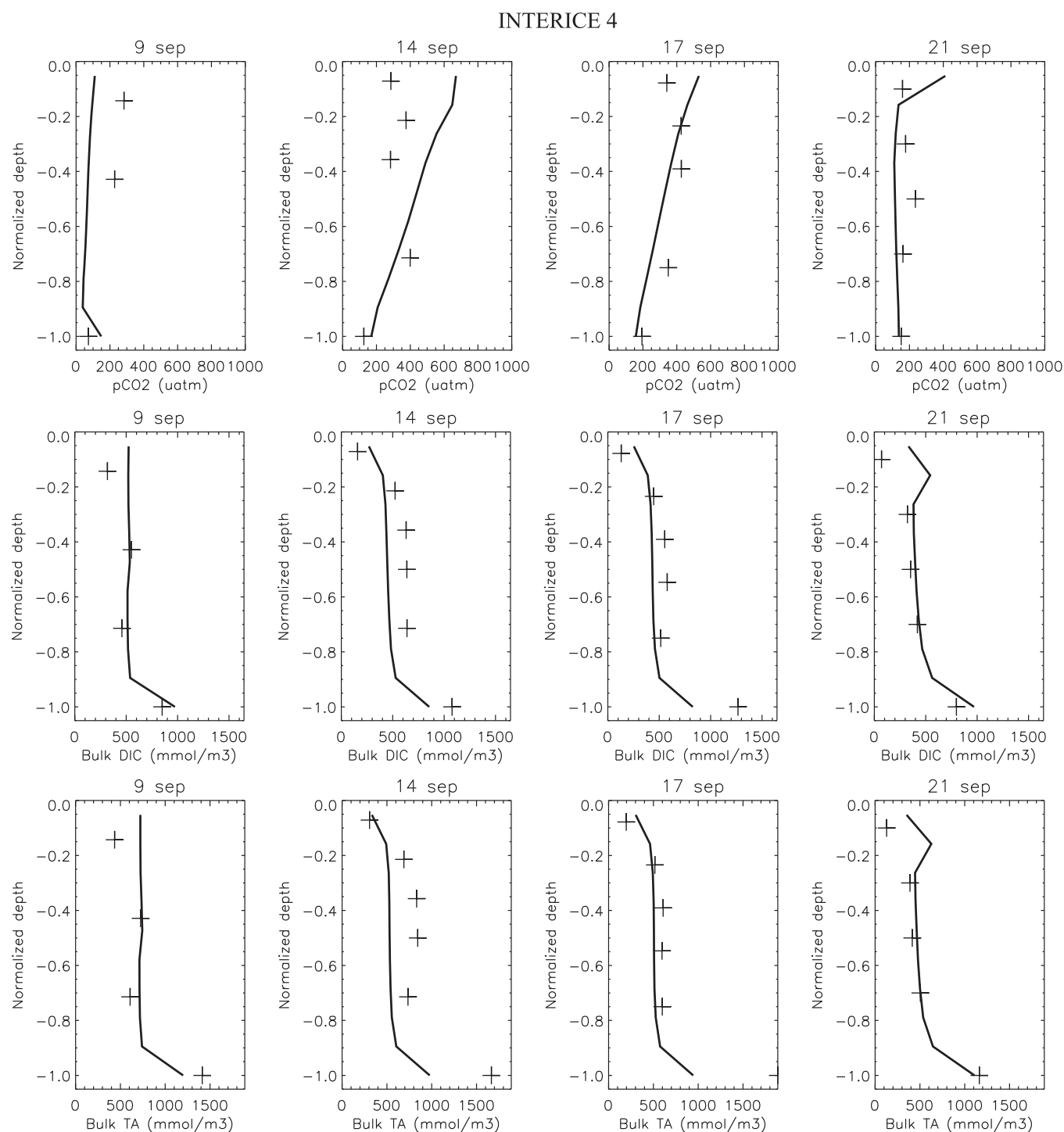


Figure 7. (μatm , top) Simulated $p\text{CO}_2$, (mmol m^{-3} , middle) bulk DIC, and bulk (mmol m^{-3} , bottom) TA normalized vertical profiles for the CTRL run for four sampling stations during the INTERICE experiment. Field observations (black crosses) are plotted for comparison with the model.

system, and hence $p\text{CO}_2$ is indeed highly sensitive to pH [Zeebe and Wolf-Gladrow, 2001]. The smaller/higher $p\text{CO}_2$ reduces/increases CO_2 fluxes in January–February compared to the CTRL (Figure 8b). Changes in TA and DIC concentrations in sea ice that do not affect the TA/DIC ratio are of smaller importance. Finally, the impact of the seawater TA/DIC ratio is smaller, since it mostly affects the $p\text{CO}_2$ near the ice base, which does not affect the surface CO_2 flux.

Table 2. Description of the Sensitivity Runs Used to Test the Role of Initial (Sea Ice) and Boundary (Seawater) DIC and TA Concentrations (mmol m^{-3}), Under Barrow Conditions^a

Run	Name	Bulk Sea Ice DIC	Bulk Sea Ice TA	Sea Ice TA/DIC	Seawater DIC	Seawater TA	Seawater TA/DIC
01	CTRL	300	400	~1.33	2000	2200	~1.1
02	Ice +20%	360	480	~1.33	2000	2200	~1.1
03	Ice -20%	240	320	~1.33	2000	2200	~1.1
04	Ice TA/DIC +20%	250	400	1.6	2000	2200	~1.1
05	Ice TA/DIC -20%	377	400	~1.06	2000	2200	~1.1
06	Seawater +10%	300	400	~1.33	2200	2400	~1.1
07	Seawater -10%	300	400	~1.33	1800	2000	~1.1
08	Seawater TA/DIC +10%	300	400	~1.33	1818.2	2200	1.21
09	Seawater TA/DIC -10%	300	400	~1.33	2222.2	2200	0.99

^aTA/DIC ratios are dimensionless.

Second, we focussed on the impact of various parameters involved in the computation of the surface CO_2 fluxes, and in particular to the boundary layer thickness z_{BL} and the permeability threshold eth . The analysis indicates, first, that the near-surface March–April $p\text{CO}_2$ (arbitrarily chosen to represent the role of winter ice-atmosphere CO_2 fluxes) increases for lower CO_2 fluxes (as simulated with $z_{BL} = 200 \mu\text{m}$) and further increases for no CO_2 flux at all (Figure 9a). In contrast, the model can hardly simulate lower near-surface $p\text{CO}_2$ and hence higher CO_2 fluxes than in the control ($z_{BL} = 0.5 \mu\text{m}$), as illustrated in Figure 9b. Decreasing z_{BL} quickly reduces the DIC stock, which brings the near-surface $p\text{CO}_2$ to values near or below the atmospheric $p\text{CO}_2$, limiting the flux. The simulated winter maximum and summer minimum CO_2 fluxes are intrinsically limited by the DIC stocks in the model, and reach an asymptote close to 1.3 and $-2.8 \text{ mmol m}^{-2} \text{ d}^{-1}$, respectively, for $z_{BL} < 0.5 \mu\text{m}$ (Figure 9b). The second important result is that, except near the surface, DIC and TA do not respond much to changes in the ice-atmosphere CO_2 flux, because those are generally small compared to the DIC stock. This is illustrated in Figures 9a and 10a for the March–April average: DIC and TA are very similar to the CTRL run when the model is run without ice-atmosphere CO_2 fluxes, with a boundary layer thickness, $z_{BL} = 200 \mu\text{m}$ (Figure 9a) or by changing the brine volume fraction permeability threshold eth (Figure 10a).

When eth is increased, the winter CO_2 efflux episodes tend to be shorter and more intense (see Figure 10b). For instance, setting $eth = 2.5\%$ leads to episodic outward CO_2 fluxes during winter (Figure 10b). The amplitude of these outward CO_2 fluxes is higher than in the CTRL ($2\text{--}10 \text{ mmol m}^{-2} \text{ d}^{-1}$). This is due to the accumulation of DIC (CO_2) near the ice surface when $e < 2.5\%$ and its subsequent release to the atmosphere when e increases above 2.5%. On the contrary, setting eth to 5% completely prevents CO_2 fluxes during ice growth (up to Julian Day 115, Figure 10b) because the near-surface brine volume is too low during ice growth. During ice melt (i.e., after Julian Day 115), CO_2 fluxes are similar between the CTRL and the two eth test runs.

Third, the model results for the March–April average $p\text{CO}_2$ and bulk DIC and TA (arbitrarily chosen to represent the role of winter ikaite precipitation) are sensitive to the precipitation and dissolution of ikaite (Figure 11a). Turning off or decreasing ($T^{\text{CaCO}_3} = 500 \text{ h}$) the timescale for ikaite precipitation decreases $p\text{CO}_2$ within the ice and increases bulk DIC and TA in the upper part of the ice where ikaite is naturally produced. By contrast, increasing the time scale for ikaite precipitation ($T^{\text{CaCO}_3} = 20 \text{ h}$) does not modify $p\text{CO}_2$, DIC, and TA in the ice. This is due to the fact that ikaite precipitation is directly limited by the supersaturation of CO_3^{2-} in brine which directly depends on DIC and TA. Hence, DIC and TA stocks provide the ultimate limitation to calcification in our simulations, which is why ikaite concentrations cannot increase indefinitely with decreasing T^{CaCO_3} . The simulated maximum concentration of ikaite produced in the model reaches an asymptote at 211 mmol m^{-3} when T^{CaCO_3} is decreased (Figure 11b).

Finally, the model results for April–May (when primary production is strongest and Chl-a accumulates in the lower half of sea ice, Figure 4) indicate that bulk DIC and TA are not very sensitive to biological activity (Figure 12). Increasing the maximum specific growth rate ($\mu_{\text{max}} \times 20$) or turning off net primary production does not significantly modify the estimation of bulk DIC and TA because the simulated primary production within sea ice is mainly nitrate limited. Indeed, the GPP integrated over the ice column and over the entire Barrow simulation is 1.3 g C m^{-2} ($108 \text{ mmol C m}^{-2}$) in the CTRL and increases only to 2.3 g C m^{-2}

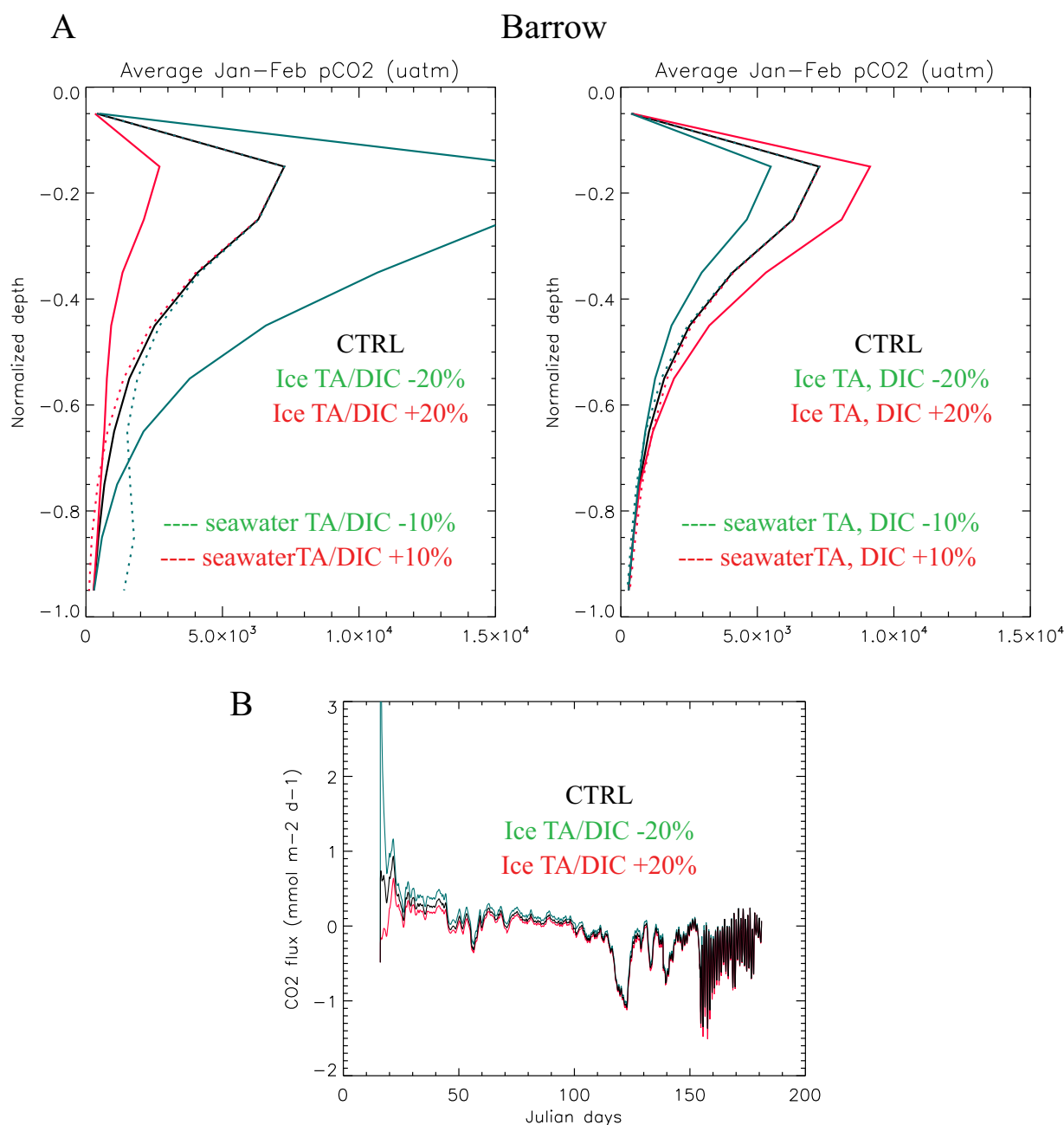


Figure 8. Sensitivity to initial and boundary conditions. (a) Simulated normalized vertical profiles of pCO₂ (uatm), at Barrow, January–February average, in the CTRL (black) and in several sensitivity runs (see Table 2). (b) Simulated sea ice-atmosphere CO₂ fluxes (mmol m⁻² d⁻¹), Barrow, in the CTRL (black), Ice TA/DIC +20% (red), and Ice TA/DIC -20% (green) simulations.

(192 mmol C m⁻²) when μ_{\max} is increased by 20. In addition, although GPP is significant compared to DIC stocks (e.g., 400 mmol m⁻² in April) in sea ice, the NPP is much smaller (79.7 mg C m⁻² (6.6 mmol C m⁻²) in the CTRL) because most of the organic carbon contained in model ice algae is respired back to DIC. This explains why the impact of biological activity on DIC and TA is small. This effect could, however, become stronger if nutrients were nonlimiting or more efficiently remineralized. In contrast, biological activity has a stronger effect on pCO₂ and O₂ dynamics in the lower half of sea ice (Figure 12). Turning off biological activity and increasing net primary production, respectively, increases and decreases the estimation of the April–May average pCO₂ profiles (Figure 12). The opposite occurs for O₂. The lower part of sea ice corresponds to where primary producers thrive.

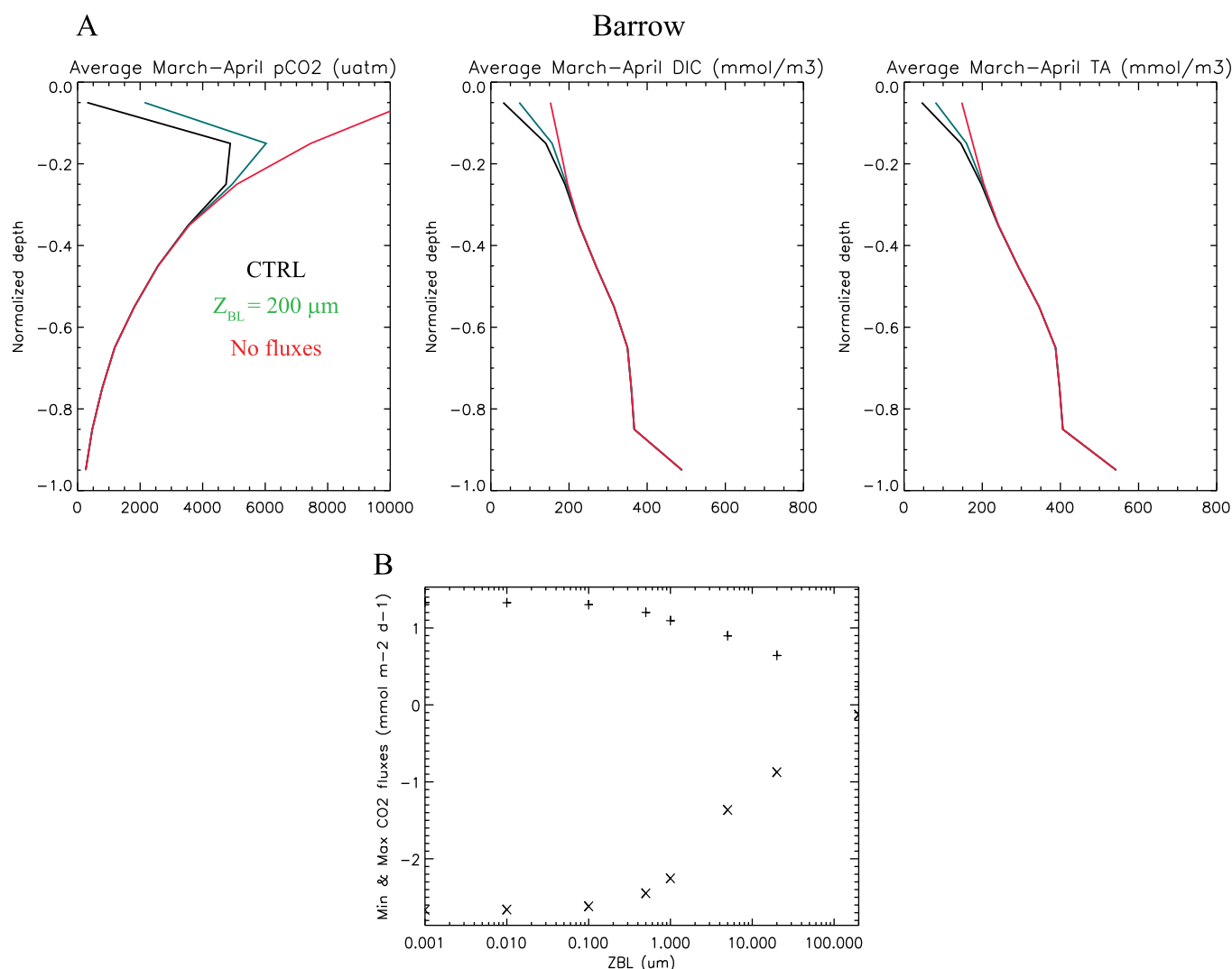


Figure 9. Sensitivity to ice-atmosphere CO₂ fluxes. (a) Simulated normalized vertical profiles of pCO₂ (uatm), DIC, and TA (mmol m⁻³), at Barrow, March–April average, in the CTRL (black), in a run with no gas fluxes (red), and in a run with the boundary layer thickness $z_{BL} = 200 \mu\text{m}$ (green) instead of $0.5 \mu\text{m}$ in the CTRL run. (b) Minimum (x) and maximum (+) simulated sea ice-atmosphere CO₂ fluxes (mmol m⁻² d⁻¹) at Barrow (Alaska) as a function of the boundary layer thickness (z_{BL} , μm).

5. Discussion

5.1. DIC Budget in Sea Ice

The analysis of the simulated DIC budget can provide pertinent information on the relative importance of the different processes driving the budget of inorganic carbon in the ice. The contributors to the DIC budget in sea ice for the simulation at Barrow are given in Figure 13. Sea ice stores oceanic DIC (mainly as HCO₃⁻) during winter and spring (i.e., January–April) while DIC is released to the underlying ocean during ice melt (i.e., June, Figure 13a). The accumulation of DIC within sea ice mainly corresponds to the entrapment during the basal formation of sea ice during winter and spring (with a maximum flux of 470.4 mmol DIC m⁻² month⁻¹ in February, Figure 13b). Most of this DIC (79% in average) is, however, rejected by brine convection to the ocean. For example, in February, we observe a peak of DIC loss to the ocean due to brine drainage of −381 mmol DIC m⁻² month⁻¹ (Figure 13b). During ice melt in May–June, brine percolation expels an important part of the sea ice DIC to the underlying ocean (−314.4 mmol DIC m⁻² month⁻¹ in June).

Biogeochemical processes contribute to a lesser extent to the budget of DIC in sea ice. During ice growth, the precipitation of CaCO₃ stores DIC under crystal form within the ice (51.1, 20.3, and 16.2 mmol DIC m⁻²

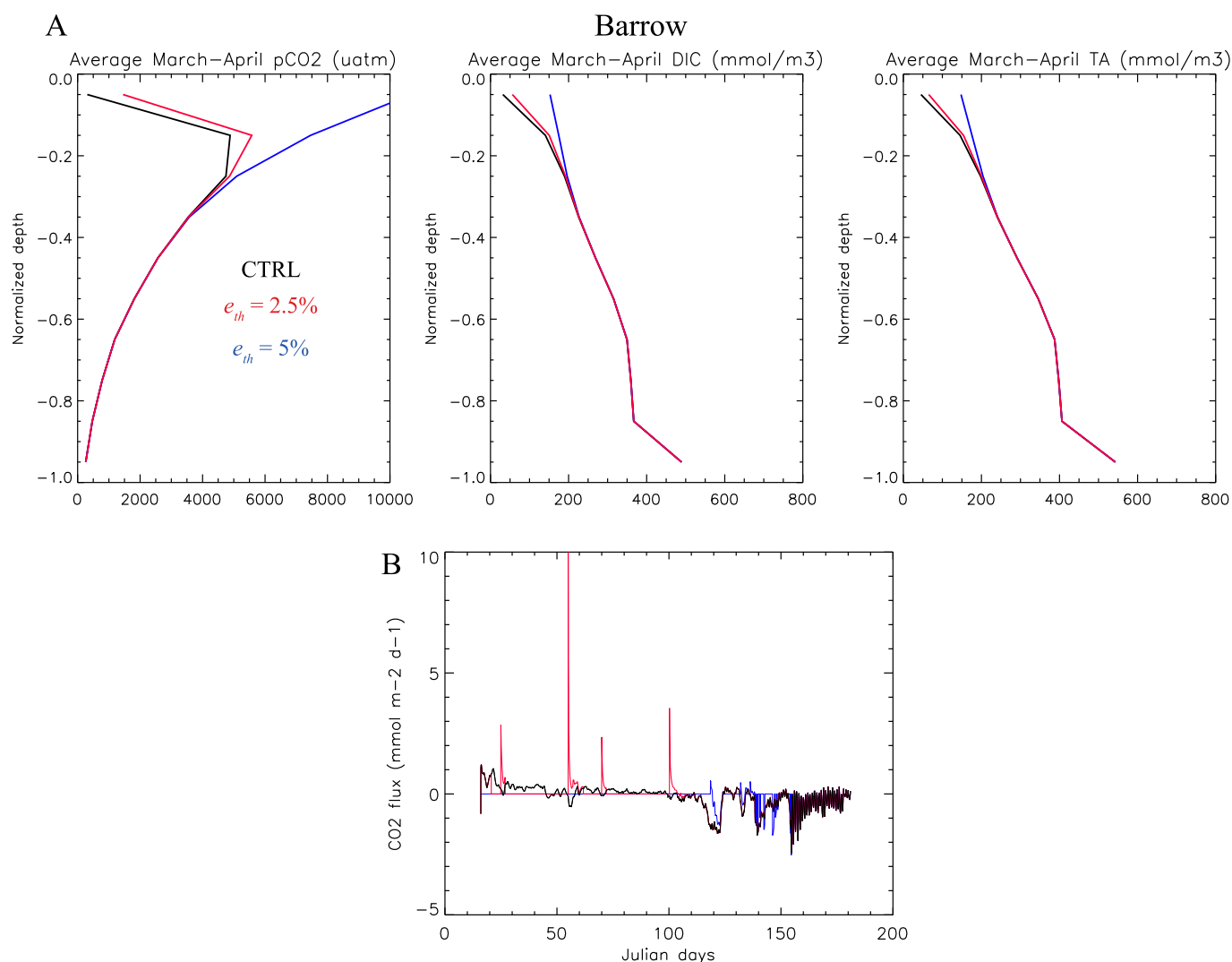


Figure 10. Sensitivity to the use of a near-surface brine volume fraction threshold e_{th} in the computation of the ice-atmosphere CO₂ flux (set to zero if $e < e_{th}$). (a) Simulated normalized vertical profiles of pCO₂ (μatm), DIC and TA (mmol m^{−3}) at Barrow, March–April average, for the CTRL run (black, for which $e_{th} = 0$), for $e_{th} = 2.5\%$ (red), and $e_{th} = 5\%$ (blue). (b) Corresponding simulated sea ice-atmosphere CO₂ fluxes (mmol m^{−2} d^{−1}).

month^{−1} in January, February, and March, respectively), and hence constitutes a sink for dissolved DIC. Ice-atmosphere CO₂ fluxes release 7.6 mmol DIC m^{−2} month^{−1} in January. During ice melt, primary production contributes to the decrease of DIC in sea ice (−48.6 and −23 mmol DIC m^{−2} month^{−1} for May and June, respectively) while some DIC is reincorporated into sea ice through respiration (49 and 26.7 mmol DIC m^{−2} month^{−1} for May and June, respectively) and atmosphere-ice CO₂ fluxes (12.4 and 10.8 mmol DIC m^{−2} month^{−1} for May and June, respectively). Meanwhile, the dissolution of CaCO₃ releases the 37.1 and 36.8 of DIC m^{−2} month^{−1} stored within the ikaite crystals back to the sea ice in April and May. The atmosphere-ice CO₂ fluxes during ice melt may seem small compared to the literature but represent the integration of the CO₂ fluxes that oscillate with the diurnal temperature cycle during ice melt (Figure 2).

The simulated DIC budget presents many similarities to that of argon (as given by Moreau *et al.* [2014]): It is dominated by the uptake of ocean DIC during growth and DIC rejection due to brine drainage. Other contributions (brine-air CO₂ fluxes, ikaite formation, and net primary production), despite significant, seem of lower importance. In contrast to argon, the release of gas bubbles to the atmosphere is not significant for DIC because of the buffering capacity of brine inclusions, which limits the amount of DIC present in gas bubbles. This all suggests that a first-order representation of the carbon budget in large-scale models must include at least the physical storage and release of DIC, whereas other processes would be of lower

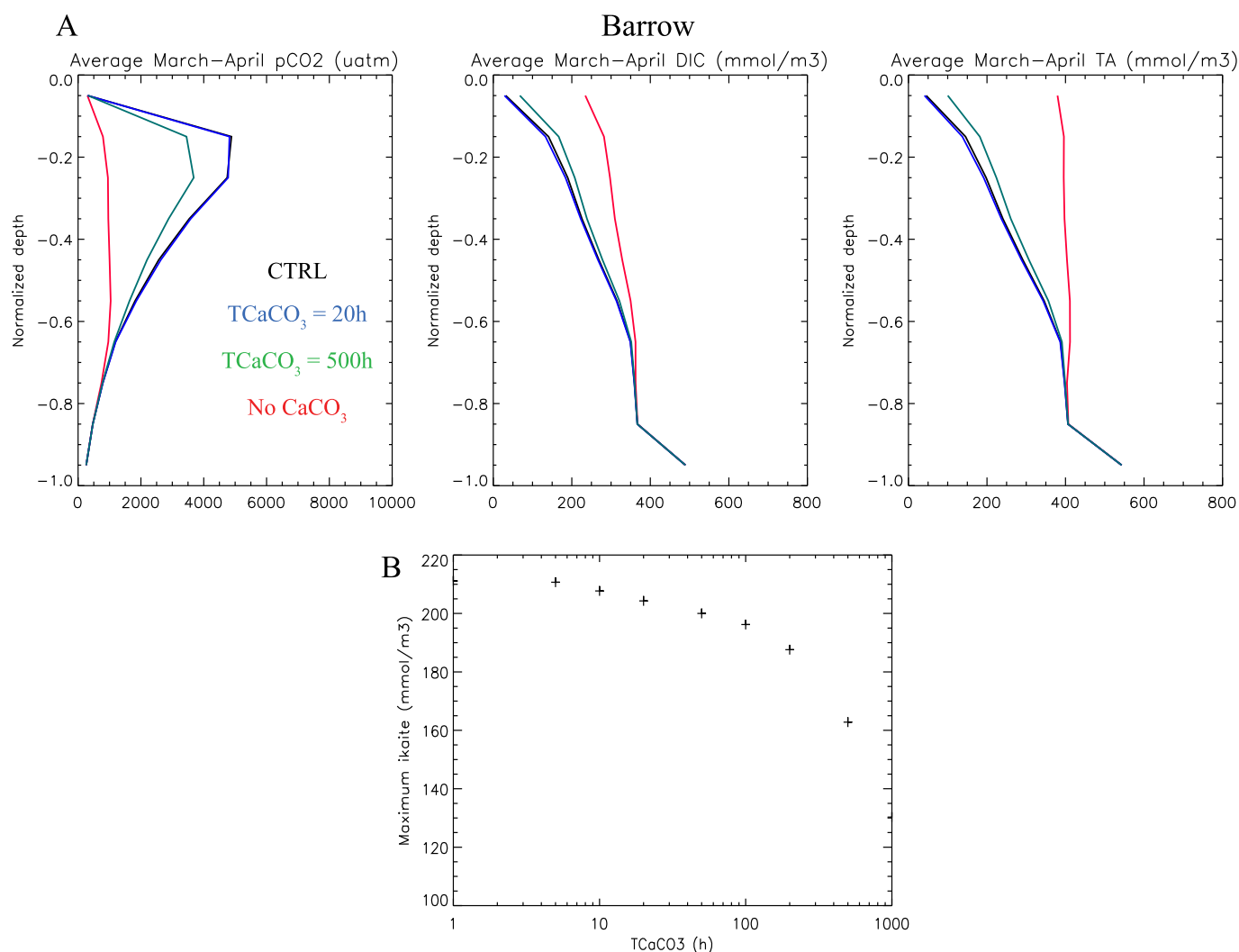


Figure 11. Sensitivity to ikaite precipitation. (a) Simulated normalized vertical profiles of pCO₂ (μatm), DIC, and TA (mmol m^{−3}), at Barrow, March–April average, for the CTRL run (black), and for runs with no CaCO₃ (red), with low (green, T_{CaCO₃} = 500 h) and high (blue, T_{CaCO₃} = 20 h) calcification. (b) Maximum simulated bulk ikaite (mmol m^{−3}) at Barrow (Alaska) as a function of T_{CaCO₃} (h).

importance. This conclusion seems valid for a reasonable number of situations, because calcification, CO₂ fluxes and net primary production are all intrinsically limited in the model. This result requires further confirmation.

5.2. Bell-Chamber Versus Eddy Covariance CO₂ Fluxes

The analyses of our simulations are a contribution to addressing the issue of why different field measurement techniques give such large differences in the estimated ice-atmosphere CO₂ fluxes. The simulated ice-atmosphere CO₂ fluxes in the CTRL run range from −2.45 to 1.2 mmol m^{−2} d^{−1} (Figure 2). These values are similar to but slightly lower than the CO₂ fluxes derived from bell-chamber techniques, ranging from −5.4 to +2 mmol m^{−2} d^{−1} [Delille et al., 2007; Geilfus et al., 2013, 2014; Nomura et al., 2010a, 2013, 2010b]. In contrast, the simulated CO₂ fluxes are inconsistent with the much higher CO₂ fluxes derived from eddy covariance (EC) techniques (−250 to 86.4 mmol m^{−2} d^{−1}, Papakyriakou and Miller [2011]; −39.3 to 19.6 mmol m^{−2} d^{−1}, Semiletov et al. [2004]).

Errors in the formulation of the ice-atmosphere fluxes could explain why simulations are inconsistent with the large observed EC fluxes. However, this does not seem to be the case since the simulated CO₂ fluxes are intrinsically limited in the model. Several attempts to increase the simulated ice-atmosphere CO₂ fluxes—for instance, by decreasing the prescribed boundary layer thickness or by adding a permeability threshold

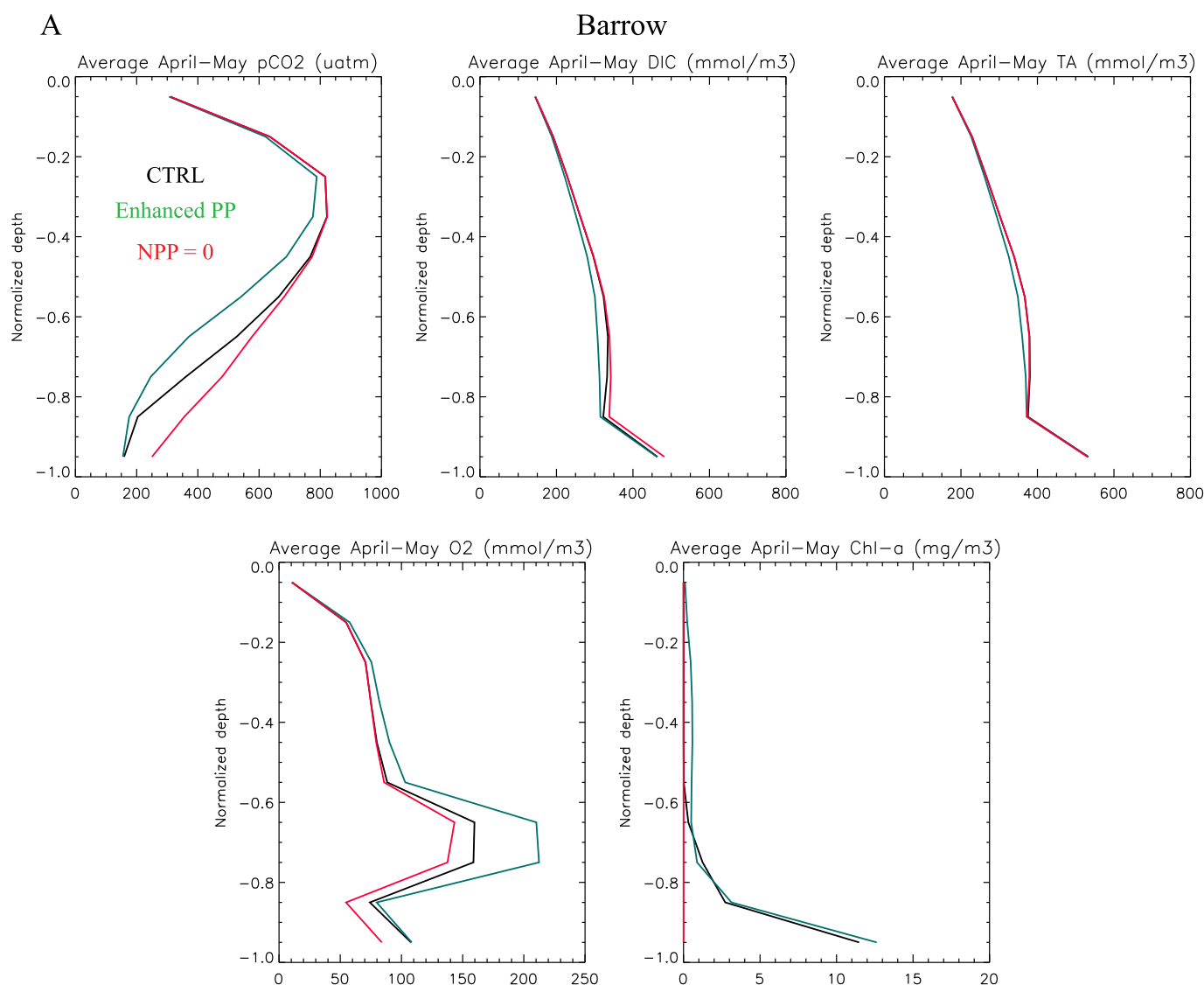


Figure 12. Sensitivity to ice algal activity. (a) Simulated normalized vertical profiles of $p\text{CO}_2$ (μatm), DIC, and TA (mmol m^{-3}), O_2 (dissolved + contained in gas bubbles, mmol m^{-3}) and Chl-a (mg m^{-3}), Barrow, April–May average, for the CTRL run (black) and runs with zero net primary production (NPP = 0, red) and enhanced primary production (green, maximum specific growth rate $\mu_{\text{max}} \times 20$).

(Figures 2, 9, and 10) —were all fruitless. In cold ice, brine volume is low, which increases the near-surface brine $p\text{CO}_2$ toward higher values than in the atmosphere, involving upwards ice-atmosphere CO_2 fluxes. In this context, forcing more intense CO_2 fluxes (e.g., by decreasing z_{BL}) quickly exhausts near-surface DIC, which decreases $p\text{CO}_2$ and hence the CO_2 flux. This cold ice limitation could partly be a model artefact. In particular, more intense winter fluxes could be obtained if brine convection transported DIC towards the ice surface, which is not the case in our model (using the formulation of Vancoppenolle *et al.* [2010]). Given the significant uncertainties in terms of simulated brine dynamics, it would be interesting to see whether other formulations for brine dynamics [e.g., Griewank and Notz, 2013; Turner *et al.*, 2013] would provide carbon pathways from the ocean toward the surface of the ice and replenish the surface ice in DIC. In summer, the increasing brine volume dilutes the brine $p\text{CO}_2$ below atmospheric values. In this set up, the CO_2 fluxes are directed downwards and limited in magnitude by the $p\text{CO}_2$ gradient, which reaches its maximum once the brine $p\text{CO}_2$ reaches 0 μatm .

If it is accepted that the intrinsic CO_2 flux limitation in the model is realistic, then the large CO_2 fluxes retrieved from the eddy covariance would likely be dominated by open water and/or ice crack-

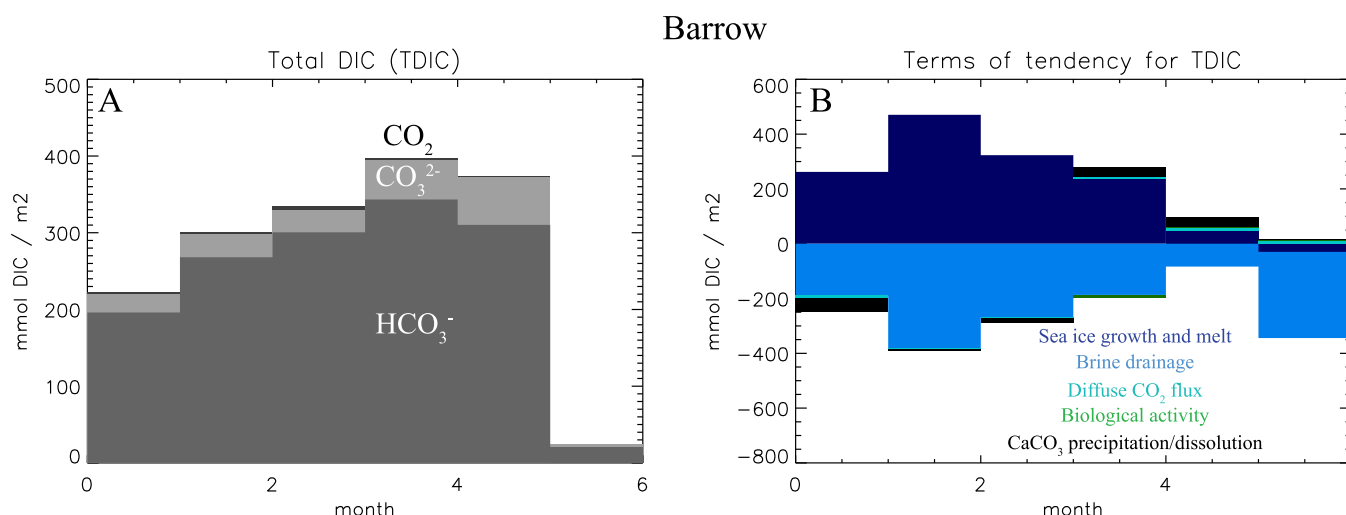


Figure 13. (a) Monthly budget of vertically averaged DIC (TDIC, mmol m⁻²) divided into CO₂ (black), CO₃²⁻ (light gray), and HCO₃⁻ (gray) for the CTRL run at Barrow. (b) Corresponding monthly mean changes (mmol m⁻² month⁻¹) in TDIC due to total sea ice growth and melt (dark blue), brine drainage (light blue), ice-atmosphere diffusive CO₂ flux (turquoise), primary production and respiration (green), and CaCO₃ precipitation and dissolution (black).

contributions, or involve other processes (e.g., surface communities, brine wicking). This is corroborated by simple calculations: for instance, if the outward eddy covariance CO₂ fluxes (19.6 mmol m⁻² d⁻¹) reported by Semiletov *et al.* [2004] represented a mean value for brine-atmosphere CO₂ fluxes, then they would entirely exhaust the sea ice DIC stock (e.g., 300 mmol m⁻² in February, Figure 13) in 15.6 days. The very high amplitude of eddy covariance CO₂ fluxes reported in the literature may also somewhat reflect the role of snow in storing and releasing gases during strong wind events as described by Colbeck [1989]. Therefore, we suggest that future studies look at the role of diffusive and wind-induced CO₂ fluxes between sea ice/cracks/leads/ponds and the atmosphere. The role of snow in these ice-atmosphere CO₂ fluxes should also be investigated.

5.3. Surface Ice Permeability and Ice-Atmosphere CO₂ Fluxes

Two questions are pertinent: which formulation of ice-atmosphere CO₂ fluxes is the most appropriate? Second, should a permeability threshold be used in the computation? Physically, several options seem plausible. That sea ice is effectively impermeable to fluid transport for brine volume fractions below 5% has long been observed [Golden *et al.*, 1998; Weeks and Ackley, 1986]. However, whether such a permeability threshold could be transposed to the brine-atmosphere dissolved gas exchange (e.g., $eth = 5\%$) is not obvious, and $eth = 0$ cannot be completely ruled out.

It is difficult to give precise recommendations as to whether or not the simulations presented here can be used to decide the value of eth . Indeed, $eth = 0$ gives CO₂ fluxes that are in the lower range of bell-chamber CO₂ flux retrievals [Delille *et al.*, 2007; Geilfus *et al.*, 2013, 2014; Nomura *et al.*, 2010a, 2013, 2010b]. $eth = 2.5\%$ gives the most realistic features: episodic CO₂ outgassing during winter and a magnitude (2–10 mmol m⁻² d⁻¹) rather closer to the observations reported in the literature (Figure 10b). $eth = 5\%$ practically prevents any CO₂ outgassing in winter, which is not realistic. However, observed and simulated near-surface brine volume fraction (e) feature uncertainties that are larger than the precision required to choose eth . The simulated near-surface brine volume fraction is underestimated by a few percent due to an intrinsic model bias in the near-surface bulk salinity [Moreau *et al.*, 2014]. Experimental retrievals have an absolute precision of a few percent, since they derive from ice bulk salinity, which itself has limited precision due to spatial variability [Eicken *et al.*, 1991] and brine loss during coring [Notz *et al.*, 2005]. Choosing eth is further complicated because no observations of the ice-atmosphere CO₂ flux are available at Barrow. Finally, the CO₂ exchange processes at the brine-atmosphere interface are not well understood. Future studies should focus on the relationship between near-surface brine volume fraction, pCO_2 , DIC, and ice-atmosphere CO₂ fluxes, e.g., from high-resolution time series.

It does not seem that uncertainties in surface permeability affect our conclusions on the CO₂ flux and DIC budget. Admittedly, increasing eth drastically increases near-surface pCO_2 and implies more intense, more

episodic outgassing events. However, such changes neither question the relatively small impact of ice-atmosphere exchanges on DIC stocks in sea ice, nor do they challenge the supposedly small footprint of ice-atmosphere CO_2 fluxes on eddy covariance CO_2 flux retrievals.

5.4. Ikaite Precipitation/Dissolution and the TA/DIC Ratio

We have good confidence in the simulated calcification rates, for several reasons: First, the newly developed calcification module could predict the laboratory observations of ikaite precipitation rates of *Papadimitriou et al.* [2014] when using a calcification time scale of $T^{\text{CaCO}_3} = 100$ h. Second, the model naturally produces higher ikaite concentrations near the ice surface (Figure 4), in agreement with the many studies reporting higher near-surface ikaite concentrations, with larger and more frequent crystals [e.g., *Rysgaard et al.*, 2013, 2014]. Finally, the simulated ikaite concentrations, up to 210 mmol m^{-3} , are in good agreement with the literature [*Dieckmann et al.*, 2008, 2010; *Fischer et al.*, 2013; *Geilfus et al.*, 2013; *Rysgaard et al.*, 2012, 2013], although they underestimate the largest values reported [e.g., *Rysgaard et al.*, 2013, 2014]. Despite this general agreement, there are other unaccounted contributors to CaCO_3 precipitation or dissolution (ionic strength, temperature, and ionic inhibitors such as orthophosphate), which were not considered here and could be important in different environments [*Papadimitriou et al.*, 2014].

More crystals grow near the surface, because they have more time to grow, and because the brine chemical conditions are more appropriate as the temperature is low there. In the lower part of the ice, the ikaite crystals are more likely to dissolve because the carbonate chemistry is closer to oceanic conditions. At Barrow, when CO_2 fluxes are turned off, less ikaite is simulated (with a maximum ikaite concentration of 129 mmol m^{-3} compared to $196.2 \text{ mmol m}^{-3}$ in the CTRL). This is consistent with the suggestion by *Papadimitriou et al.* [2013, 2014] that CO_2 removal through primary production and/or ice-atmosphere fluxes, would increase brine pH, and therefore, favor ikaite precipitation in sea ice.

It is of interest as to why the largest CaCO_3 concentrations reported in the literature are not reproduced in the model. Field measurements of ikaite range from 15 to $\sim 900 \text{ mmol m}^{-3}$ [*Dieckmann et al.*, 2008, 2010; *Fischer et al.*, 2013; *Geilfus et al.*, 2013; *Rysgaard et al.*, 2012, 2013]. In the model, the maximum ikaite concentration was limited, reaching an asymptotic maximum near 210 mmol m^{-3} when trying to increase calcification (i.e., when T^{CaCO_3} is decreased, Figure 11b). The model ikaite precipitation is controlled by the saturation of CO_3^{2-} , thus by changes in pH and salinity [*Hu et al.*, 2014; *Papadimitriou et al.*, 2013, 2014], but the ultimate limitation comes from TA and DIC stocks. Indeed, increasing the initial bulk DIC and TA concentrations in sea ice by 20% leads to a maximum ikaite concentration of $238.5 \text{ mmol m}^{-3}$. Hence, we suggest that the high values (e.g., above 250 mmol m^{-3}) reported in the literature result from processes that are not represented in the model (e.g., frost flowers, brine skim, see *Rysgaard et al.* [2014]).

It is questionable if *nonfiltered* TA/DIC ratios near ~ 2 are reliable indirect indicators of ikaite precipitation in sea ice, as suggested in the literature [*Rysgaard et al.*, 2009, 2007], or rather that such ratios reflect outgassing or primary production [*Papadimitriou et al.*, 2007]. To answer that question, the sensitivity of the *nonfiltered* TA/DIC ratio to the absence of various processes in the model was investigated (Figure 14). In the CTRL run, the TA/DIC ratio is reasonable, with values generally above >1 during the cold season (from January to April), increasing up to ~ 2 near the ice surface (Figures 4 and 14). The sensitivity runs suggest that TA/DIC ratio of ~ 2 is mainly the signature of outgassing, decreasing DIC and keeping TA constant. CaCO_3 also contributes to increase the near-surface *nonfiltered* TA/DIC ratio, but less so, whereas the impact of biological activity is negligible.

6. Conclusions

Using a one-dimensional thermodynamic sea ice model including brine dynamics, brine-atmosphere CO_2 exchanges, calcification, and biological activity, we investigate inorganic carbon dynamics observed during the seasonal growth and decay of landfast sea ice near Barrow on the Northern Alaskan Coast and in a 2 weeks laboratory ice tank experiment (INTERICE 4). The uncertainties related to the model representations of ice-atmosphere gas exchange and calcification were constrained by a thorough observation-based evaluation of the model and numerous sensitivity experiments. Since the simulations are consistent with observations (in terms of DIC and TA concentrations, CO_2 fluxes, calcification and biological activity), we are

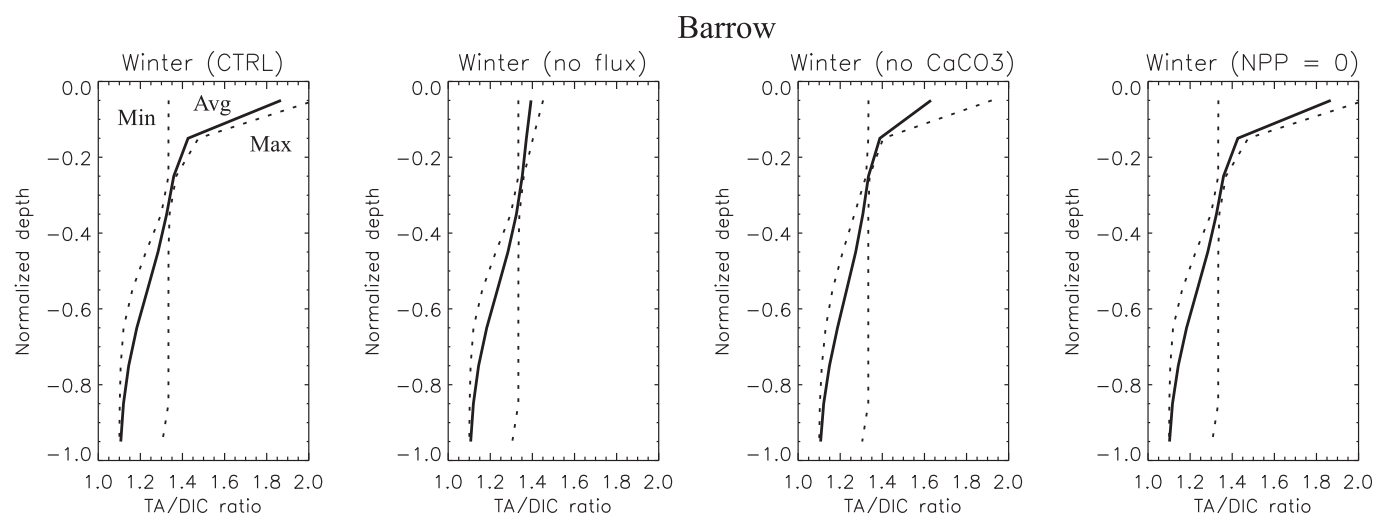


Figure 14. Normalized vertical profile of the *nonfiltered* TA/DIC ratio (solid: winter mean; dots: min and max) at Barrow, for the CTRL, and for several sensitivity runs: no ice-atmosphere CO_2 flux, no CaCO_3 and no NPP.

confident in their ability to represent the main features of inorganic carbon dynamics in sea ice. Based on the analysis of model, the following conclusions can be drawn:

1. At Barrow, the inorganic carbon budget in seasonal ice is mostly driven by physical processes, reflecting the balance between DIC uptake in growing ice, which is not fully compensated by the rejection of DIC in seawater through brine convection. Other processes such as ice-atmosphere CO_2 fluxes, calcification and biological activity, despite being significant, seem of less importance in terms of DIC budget.
2. In terms of ice-atmosphere CO_2 exchanges, sea ice is a net CO_2 source during ice growth and a net CO_2 sink during ice melt.
3. The formulation of the ice-atmosphere CO_2 flux is characterized by large uncertainties, which mostly affect the simulated near-surface $p\text{CO}_2$ and the ice-atmosphere CO_2 fluxes. However, this does not strongly affect the carbon budget, because the contribution of ice-atmosphere fluxes to the DIC budget is relatively small.
4. Small ice-atmosphere CO_2 fluxes and their intrinsic limitation by DIC stocks in the ice and by air-brine $p\text{CO}_2$ gradients suggest that the relatively large CO_2 fluxes retrieved from eddy covariance method cannot be explained solely by a sea ice direct source and must involve other processes (e.g., gas storage in snow, surface communities, brine wicking) or other sources of CO_2 (e.g., cracks in the ice, leads and open water).
5. Near-surface TA/DIC ratios of ~ 2 , which are sometimes used as indicators for calcification, are rather suggested to be indicative of outgassing.

Appendix A: Primary Production in the Model

The photosynthesis/respiration model we use here is a classical nutrient-phytoplankton (N-P) module. It includes one ice algae group (diatoms) and two potentially limiting nutrients (nitrate + nitrite and silicate).

Net primary production (NPP, in carbon units) is formulated as:

$$\text{NPP} = \text{GPP} - \text{respiration}$$

Gross primary production (GPP) is proportional to the carbon content of diatoms and limited by light [Platt and Jassby, 1976], nutrients [Monod, 1949] and inhibited by low temperature [Eppley, 1972] and high brine salinity [Arrigo and Sullivan, 1992]. The respiration rate is directly proportional to ice algal biomass. Chl-a is diagnosed from ice algal carbon concentrations, and light attenuation depends on Chl-a concentration [Arrigo et al., 1991]. This N-P module is coupled to brine transport: nutrients are treated as dissolved tracers, moving with brine motion, whereas ice algae are treated as motionless particulate tracers. As shown in the

text, the vertical Chl-*a* profile and the timing and magnitude of primary production in this model are reasonable, as well as the location of ice algal communities, which is sufficient for the focus of the present paper: this N-P model is used here as an external constraint to determine the potential role of biological activity on carbon dynamics in sea ice. Finally, oxygen (O₂) concentrations are also simulated in this model. As for argon in Moreau *et al.* [2014], O₂ is assumed to be a gas tracer (including dissolved and gas bubble phases), produced by photosynthesis and consumed by respiration (following the Redfield ratio).

Acknowledgments

We want to thank our funding sources and partners: the F.R.S.-FNRS (FRFC grant 2.4649.07), the Belgian Science Federal Policy Office (BIGSOUTH project), the European Union (via the projects BISICLO, FP7 CIG 321938, and HYDRALAB III, FP6 022441 RII3), the MARE project, and BEPSII (Biogeochemical Exchange Processes at the Sea Ice Interfaces, SCOR Working Group 140). Special thanks go to the personnel of the Hamburg Ship Model Basin (HSVA), especially Kalle Evers and the ice tank crew, for the hospitality, technical and scientific support, and the professional execution of the test programme in the Research Infrastructure ARCTECLAB. We also thank Erica Allhusen and Gerhard Dieckmann, AWI, for arranging the supply of seawater, and other logistic support, for the INTERICE 4 experiment. The authors are also grateful to France Deleu and Alan Willame who performed a large part of the measurements. H. G., B. D., S. M., and J. Z. are senior research associate, research associate, postdoctoral researcher, and research fellow with the F.R.S.-FNRS. N. X. G. acknowledges the Canada Excellence Research Chair Program and is supported by a grant from the Arctic Research Center, Aarhus University, Aarhus, Denmark. The observation data and the model code will be made available to any scientist upon request and encouraged in order to reproduce and test the model results in other locations (contacts: s.moreau@uclouvain.be and martin.vancoppenolle@ocean-ipsl.upmc.fr). Finally, we would like to thank Nadja Steiner and one anonymous reviewer for their very valuable and constructive comments.

References

- Arrigo, K., and C. W. Sullivan (1992), The influence of salinity and temperature covariation on the photophysiological characteristics of Antarctic sea ice microalgae, *J. Phycol.*, **28**(6), 746–756.
- Arrigo, K., C. W. Sullivan, and J. N. Kremer (1991), A bio-optical model of Antarctic sea ice, *J. Geophys. Res.*, **96**(C6), 10,581–10,592.
- Arrigo, K., T. Mock, and M. Lizotte (2010), Primary producers and sea ice, in *Sea Ice*, edited by D. N. Thomas and G. S. Dieckmann, pp. 282–325, Wiley-Blackwell, Oxford, U. K.
- Assur, A. (1958), Composition of sea ice and its tensile strength, in *Arctic Sea Ice*, edited, pp. 106–138, U.S. Natl. Acad. of Sci.—Natl. Res. Council, Publ., Washington, D. C.
- Bates, N. R. (2006), Air-sea CO₂ fluxes and the continental shelf pump of carbon in the Chukchi Sea adjacent to the Arctic Ocean, *J. Geophys. Res.*, **111**, C10013, doi:10.1029/2005JC003083.
- Bitz, C. M., and W. H. Lipscomb (1999), An energy-conserving thermodynamic model of sea ice, *J. Geophys. Res.*, **104**(C7), 15,669–15,677.
- Broecker, W. S., and T. H. Peng (1974), Gas exchange rates between air and sea, *Tellus*, **26**, 21–35.
- Brown, K. A., L. A. Miller, M. Davelaar, R. Francois, and P. D. Tortell (2014), Over-determination of the carbonate system in natural sea-ice brine and assessment of carbonic acid dissociation constants under low temperature, high salinity conditions, *Mar. Chem.*, **165**, 36–45, doi:10.1016/j.marchem.2014.07.005.
- Colbeck, S. C. (1989), Air movement in snow due to windpumping, *J. Glaciol.*, **35**(120), 209–213.
- Crabeck, O., B. Delille, S. Rysgaard, D. N. Thomas, N.-X. Geilfus, B. G. T. Else, and J.-L. Tison (2014), First ‘in situ’ determination of gas transport coefficients (DO₂, DAr and DN₂) from bulk gas concentration measurements (O₂, N₂, Ar) in natural sea ice, *J. Geophys. Res. Oceans*, **119**, 6655–6668, doi:10.1002/2014JC009849.
- Deal, C., M. Jin, S. Elliott, E. Hunke, M. Maltrud, and N. Jeffery (2011), Large-scale modeling of primary production and ice algal biomass within arctic sea ice in 1992, *J. Geophys. Res.*, **116**, C07004, doi:10.1029/2010JC006409.
- Delille, B. (2006), *Inorganic Carbon Dynamics and Air-Ice-Sea CO₂ Fluxes in the Open and Coastal Waters of the Southern Ocean*, 296 pp., Univ. de Liège, Liège, Belgium.
- Delille, B., B. Jourdain, A. V. Borges, J. L. Tison, and D. Delille (2007), Biogas (CO₂, O₂, dimethylsulfide) dynamics in spring Antarctic fast ice, *Limnol. Oceanogr. Methods*, **52**(4), 1367–1379, doi:10.4319/lo.2007.52.4.1367.
- Delille, B., et al. (2014), Southern Ocean CO₂ sink: The contribution of the sea ice, *J. Geophys. Res. Oceans*, **119**, 6340–6355, doi:10.1002/2014JC009941.
- Dickson, A. G., and F. J. Millero (1987), A comparison of the equilibrium constants for the dissociation of carbonic acid in seawater media, *Deep Sea Res., Part A*, **34**(10), 1733–1743.
- Dieckmann, G. S., G. Nehrke, S. Papadimitriou, J. Göttlicher, R. Steininger, H. Kennedy, D. Wolf-Gladrow, and D. N. Thomas (2008), Calcium carbonate as ikaite crystals in Antarctic sea ice, *Geophys. Res. Lett.*, **35**, L08501, doi:10.1029/2008GL033540.
- Dieckmann, G. S., G. Nehrke, C. Uhlig, J. Göttlicher, S. Gerland, M. A. Granskog, and D. N. Thomas (2010), Brief communication: Ikaite (CaCO₃·6H₂O) discovered in Arctic sea ice, *Cryosphere*, **4**, 227–230.
- Eicken, H., M. A. Lange, and G. S. Dieckmann (1991), Spatial variability of sea ice properties in the northwestern Weddell Sea, *J. Geophys. Res.*, **96**(C6), 10,603–10,615.
- Eppley, R. W. (1972), Temperature and phytoplankton growth in the sea, *Fish Bull.*, **70**, 1063–1085.
- Fischer, M., D. N. Thomas, A. Krell, G. Nehrke, J. Göttlicher, L. Norman, K. M. Meiners, C. Riaux-Gobin, and G. S. Dieckmann (2013), Quantification of ikaite in Antarctic sea ice, *Antarct. Sci.*, **25**(3), 421–432.
- Geilfus, N. X., B. Delille, V. Verbeke, and J. L. Tison (2012), Towards a method for high vertical resolution measurements of the partial pressure of CO₂ within bulk sea ice, *J. Glaciol.*, **58**(208), 287–300, doi:10.3189/2012JoG11J071.
- Geilfus, N. X., G. Carnat, G. S. Dieckmann, N. Halden, G. Nehrke, T. Papakyriakou, J. L. Tison, and B. Delille (2013), First estimates of the contribution of CaCO₃ precipitation to the release of CO₂ to the atmosphere during young sea ice growth, *J. Geophys. Res. Oceans*, **118**, 244–255, doi:10.1029/2012JC007980.
- Geilfus, N. X., R. J. Galley, O. Crabeck, T. Papakyriakou, J. Landy, J. L. Tison, and S. Rysgaard (2014), Inorganic carbon dynamics of melt pond-covered first year sea ice in the Canadian Arctic, *Biogeosci. Discuss.*, **11**(5), 7485–7519, doi:10.5194/bgd-11-7485-2014.
- Golden, K. M., S. F. Ackley, and V. I. Lytle (1998), The percolation phase transition in sea ice, *Science*, **282**(5397), 2238–2241, doi:10.1126/science.282.5397.2238.
- Griewank, P. J., and D. Notz (2013), Insights into brine dynamics and sea ice desalination from a 1-D model study of gravity drainage, *J. Geophys. Res. Oceans*, **118**, 3370–3386, doi:10.1002/jgrc.20247.
- Hu, Y. B., D. A. Wolf-Gladrow, G. S. Dieckmann, C. Völker, and G. Nehrke (2014), A laboratory study of ikaite (CaCO₃·6H₂O) precipitation as a function of pH, salinity, temperature and phosphate concentration, *Mar. Chem.*, **162**, 10–18.
- Light, B., G. A. Maykut, and T. C. Grenfell (2003), Effects of temperature on the microstructure of first-year Arctic sea ice, *J. Geophys. Res.*, **108**(C2), 3051, doi:10.1029/2001JC000887.
- Loose, B., L. A. Miller, S. Elliott, and T. Papakyriakou (2011), Sea ice biogeochemistry and material transport across the frozen interface, *Oceanography*, **24**(3), 202–218, doi:10.5670/oceanog.2011.72.
- Maykut, G. A., and N. Untersteiner (1971), Some results from a time-dependent thermodynamic model of sea ice, *J. Geophys. Res.*, **76**(6), 1550–1575.
- Mehrbach, C., C. H. Culbertson, J. E. Hawley, and R. N. Pytkowicz (1973), Measurement of the apparent dissociation constants of carbonic acid in seawater at atmospheric pressure, *Limnol. Oceanogr.*, **18**, 897–907.
- Miller, L. A., T. N. Papakyriakou, R. E. Collins, J. W. Deming, J. K. Ehn, R. W. MacDonald, A. Mucci, O. Owens, M. Raudsepp, and N. Sutherland (2011), Carbon dynamics in sea ice: A winter flux time series, *J. Geophys. Res.*, **116**, C02028, doi:10.1029/2009JC006058.
- Monod, J. (1949), The growth of bacterial cultures, *Annu. Rev. Microbiol.*, **3**, 371–394.

- Morales Maqueda, M. A., and S. Rahmstorf (2002), Did Antarctic sea-ice expansion cause glacial CO₂ decline?, *Geophys. Res. Lett.*, **29**(1), 1011, doi:10.1029/2001GL013240.
- Moreau, S., M. Vancoppenolle, J. Zhou, J.-L. Tison, B. Delille, and H. Goosse (2014), Modeling Argon dynamics in first-year sea ice, *Ocean Modell.*, **73**, 1–18.
- Nomura, D., H. Yoshikawa-Inoue, and T. Toyota (2006), The effect of sea-ice growth on air-sea CO₂ flux in a tank experiment, *Tellus, Ser. B*, **58**(5), 418–426, doi:10.1111/j.1600-0889.2006.00204.x.
- Nomura, D., H. Eicken, R. Gradingier, and K. Shirasawa (2010a), Rapid physically driven inversion of the air-sea ice CO₂ flux in the seasonal landfast ice off Barrow, Alaska after onset of surface melt, *Cont. Shelf Res.*, **30**(19), 1998–2004, doi:10.1016/j.csr.2010.09.014.
- Nomura, D., H. Yoshikawa-Inoue, T. Toyota, and K. Shirasawa (2010b), Effects of snow, snowmelting and refreezing processes on air-sea-ice CO₂ flux, *J. Glaciol.*, **56**(196), 262–270, doi:10.3189/002214310791968548.
- Nomura, D., M. A. Granskog, P. Assmy, D. Simizu, and G. Hashida (2013), Arctic and Antarctic sea ice acts as a sink for atmospheric CO₂ during periods of snowmelt and surface flooding, *J. Geophys. Res. Oceans*, **118**, 6511–6524, doi:10.1002/2013JC009048.
- Notz, D. (2005), *Thermodynamic and Fluid-Dynamical Processes in Sea Ice*, Univ. of Cambridge, Cambridge, U. K.
- Notz, D., J. S. Wettlaufer, and M. G. Worster (2005), Instruments and methods: A non-destructive method for measuring the salinity and solid fraction of growing sea ice in situ, *J. Glaciol.*, **51**(172), 159–166.
- Orr, J. C., et al. (2001), Estimates of anthropogenic carbon uptake from four three-dimensional global ocean models, *Global Biogeochem. Cycles*, **15**(1), 43–60.
- Papadimitriou, S., H. Kennedy, G. Kattner, G. S. Dieckmann, and D. N. Thomas (2003), Experimental evidence for carbonate precipitation and CO₂ degassing during sea ice formation, *Geochim. Cosmochim. Acta*, **68**(8), 1749–1761, doi:10.1016/j.gca.2003.07.004.
- Papadimitriou, S., D. N. Thomas, H. Kennedy, C. Haas, H. Kuosa, A. Krell, and G. S. Dieckmann (2007), Biogeochemical composition of natural sea ice brines from the Weddell Sea during early austral summer, *Limnol. Oceanogr. Methods*, **52**(5), 1809–1823, doi:10.4319/lo.2007.52.5.1809.
- Papadimitriou, S., H. Kennedy, P. Kennedy, and D. N. Thomas (2013), Ikaite solubility in seawater-derived brines at 1atm and sub-zero temperatures to 265K, *Geochim. Cosmochim. Acta*, **109**, 241–253.
- Papadimitriou, S., H. Kennedy, P. Kennedy, and D. N. Thomas (2014), Kinetics of ikaite precipitation and dissolution in seawater-derived brines at sub-zero temperatures to 265 K, *Geochim. Cosmochim. Acta*, **140**, 199–211, doi:10.1016/j.gca.2014.05.031.
- Papakyriakou, T., and L. Miller (2011), Springtime CO₂ exchange over seasonal sea ice in the Canadian Arctic Archipelago, *Ann. Glaciol.*, **52**(57 Part 2), 215–224, doi:10.3189/172756411795931534.
- Platt, T., and A. D. Jassby (1976), The relationship between photosynthesis and light for natural assemblages of coastal marine phytoplankton, *J. Phycol.*, **12**, 421–430.
- Qian, J., and K. Mopper (1996), High performance high temperature combustion total organic carbon analyzer, *Anal. Chem.*, **68**, 3090–3097.
- Redfield, A. C., B. H. Ketchum, and F. A. Richards (1963), The influence of organisms on the composition of seawater, in *The Sea*, edited by M. N. Hill, pp. 26–77, Interscience, N. Y.
- Romanek, C. S., E. L. Grossman, and J. W. Morse (1992), Carbon isotopic fractionation in synthetic calcite and aragonite: Effects of temperature and precipitation rate, *Geochim. Cosmochim. Acta*, **56**, 419–430.
- Rysgaard, S., R. N. Glud, M. K. Sejr, J. Bendtsen, and P. B. Christensen (2007), Inorganic carbon transport during sea ice growth and decay: A carbon pump in polar seas, *J. Geophys. Res.*, **112**, C03016, doi:10.1029/2006JC003572.
- Rysgaard, S., J. Bendtsen, L. T. Pedersen, H. Ramtøv, and R. N. Glud (2009), Increased CO₂ uptake due to sea ice growth and decay in the Nordic Seas, *J. Geophys. Res.*, **114**, C09011, doi:10.1029/2008JC005088.
- Rysgaard, S., J. Bendtsen, B. Delille, G. S. Dieckmann, R. N. Glud, H. Kennedy, J. Mortensen, S. Papadimitriou, D. N. Thomas, and J. L. Tison (2011), Sea ice contribution to the air-sea CO₂ exchange in the Arctic and Southern Oceans, *Tellus, Ser. B*, **63**(5), 823–830, doi:10.1111/j.1600-0889.2011.00571.x.
- Rysgaard, S., R. N. Glud, K. Lennert, M. Cooper, N. Halden, R. J. G. Leakey, F. C. Hawthorne, and D. Barber (2012), Ikaite crystals in melting sea ice—Implications for pCO₂ and pH levels in Arctic surface waters, *Cryosphere*, **6**(4), 901–908, doi:10.5194/tc-6-901-2012.
- Rysgaard, S., et al. (2013), Ikaite crystal distribution in Arctic winter sea ice and implications for CO₂ system dynamics, *Cryosphere*, **7**, 707–718.
- Rysgaard, S., et al. (2014), Temporal dynamics of ikaite in experimental sea ice, *Cryosphere*, **8**, 1469–1478.
- Sarmiento, J. L., and N. Gruber (2006), *Ocean Biogeochemical Dynamics*, Princeton Univ. Press, Princeton, N. J.
- Semiletov, I., A. Makshtas, S. I. Akasofu, and E. L. Andreas (2004), Atmospheric CO₂ balance: The role of Arctic sea ice, *Geophys. Res. Lett.*, **31**, L05121, doi:10.1029/2003GL017996.
- Stephens, B. B., and R. F. Keeling (2000), The influence of Antarctic sea ice on glacial-interglacial CO₂ variations, *Nature*, **404**, 171–174.
- Thomas, D. N., and G. S. Dieckmann (2002), Antarctic sea ice: A habitat for extremophiles, *Science*, **295**, 641–644.
- Thomas, D. N., et al. (1998), Biological soup within decaying summer sea ice in the Amudsen Sea, Antarctica, in *Antarctic Sea Ice Biological Processes, Interactions, and Variability*, *Antart. Res. Ser.*, vol. 73, edited by M. P. Lizotte and K. Arrigo, pp. 161–171, AGU, Washington, D. C.
- Thomas, D. N., G. S. Dieckmann, R. Engbrodt, V. Giannelli, G. Kattner, H. Kennedy, C. Haas, and G. S. Dieckmann (2001a), Dissolved organic matter in Antarctic sea ice, *Ann. Glaciol.*, **33**, 297–303.
- Thomas, D. N., G. S. Dieckmann, R. Engbrodt, V. Giannelli, G. Kattner, H. Kennedy, C. Haas, and G. S. Dieckmann (2001b), Biogeochemistry of platelet ice: Its influence on particle flux under fast ice in the Weddell Sea, Antarctica, *Pol. Biol.*, **24**, 486–496.
- Tison, J. L., C. Haas, M. M. Gowing, S. Sleewaegen, and A. Bernard (2002), Tank study of physico-chemical controls on gas content and composition during growth of young sea ice, *J. Glaciol.*, **48**(161), 177–190.
- Turner, A. K., E. C. Hunke, and C. M. Bitz (2013), Two modes of sea-ice gravity drainage: A parameterization for large-scale modeling, *J. Geophys. Res. Oceans*, **118**(5), 2279–2294, doi:10.1002/jgrc.20171.
- Vancoppenolle, M., C. M. Bitz, and T. Fichefet (2007), Summer landfast sea ice desalination at Point Barrow, Alaska: Modeling and observations, *J. Geophys. Res.*, **112**, C04022, doi:10.1029/2006JC003493.
- Vancoppenolle, M., H. Goosse, A. De Montety, T. Fichefet, B. Tremblay, and J. L. Tison (2010), Modeling brine and nutrient dynamics in Antarctic sea ice: The case of dissolved silica, *J. Geophys. Res.*, **115**, C02005, doi:10.1029/2009JC005369.
- Vancoppenolle, M., et al. (2013), Large-scale interactions between sea ice and polar marine biogeochemistry: Emerging views on the relevant processes and their modelling, *Quat. Sci. Rev.*, **79**, 207–230.
- Weeks, W., and S. Ackley (1982), *The Growth, Structure and Properties of Sea Ice*, *CRREL Monogr.*, vol. 82-1, Cold Reg., Res. and Eng. Lab., Hanover, N. H.
- Weeks, W., and S. Ackley (1986), The growth, structure and properties of sea ice, in *Eophysics of Sea Ice*, *CRREL Monogr.*, vol. 82-1, edited by N. Untersteiner, pp. 9–164, Plenum Press, London, U. K.

- Weiss, R. F. (1974), Carbon dioxide in water and seawater: The solubility of a non-ideal gas, *Mar. Chem.*, 2(3), 203–215.
- Weissenberger, J. (1992), The environmental conditions in the brine channels of Antarctic sea ice, *Rep. Pol. Res.*, 111, 1–159.
- Zeebe, R. E., and D. Wolf-Gladrow (2001), *CO₂ in Seawater: Equilibrium, Kinetics, Isotopes*, 346 pp., Elsevier, Amsterdam.
- Zemmelink, H. J., B. Delille, J. L. Tison, E. J. Hintsa, L. Houghton, and J. W. H. Dacey (2006), CO₂ deposition over the multi-year ice of the western Weddell Sea, *Geophys. Res. Lett.*, 33, L13606, doi:10.1029/2006GL026320.
- Zhou, J., B. Delille, N.-X. Geilfus, F. Brabant, H. Eicken, G. Carnat, M. Vancoppenolle, and J.-L. Tison (2013), Physical and biogeochemical properties in landfast sea ice (Barrow, Alaska): Insights on brine and gas dynamics across seasons, *J. Geophys. Res. Oceans*, 118, 3172–3189, doi:10.1002/jgrc.20232.